The Astrophysical Journal, 909:56 (25pp), 2021 March 1 https://doi.org/10.3847/1538-4357/abd801

CO Excitation, Molecular Gas Density, and Interstellar Radiation Field in Local and High-redshift Galaxies

Daizhong Liu[1], Emanuele Daddi[2], Eva Schinnerer[1], Toshiki Saito[1], Adam Leroy[3], John D. Silverman[4,5], Francesco Valentino[6,7], Georgios E. Magdis[6,7,8,9], Yu Gao[10,11], Shuowen Jin[12,13], Annagrazia Puglisi[14], and Brent Groves[15,16]

[1] Max Planck Institute for Astronomy, Königstuhl 17, D-69117 Heidelberg, Germany; dzliu@mpia.de
[2] CEA, Irfu, DAp, AIM, Universitè Paris-Saclay, Universitè de Paris, CNRS, F-91191 Gif-sur-Yvette, France
[3] 18 Department of Astronomy, The Ohio State University, 140 West 18th Ave., Columbus, OH 43210, USA
[4] Kavli Institute for the Physics and Mathematics of the Universe, The University of Tokyo (Kavli IPMU, WPI), Kashiwa 277-8583, Japan
[5] Department of Astronomy, School of Science, The University of Tokyo, 7-3-1 Hongo, Bunkyo, Tokyo 113-0033, Japan
[6] Cosmic Dawn Center (DAWN), Copenhagen, Denmark
[7] Niels Bohr Institute, University of Copenhagen, Jagtvej 128 DK-2200 Copenhagen N, Denmark
[8] DTU-Space, Technical University of Denmark, Elektrovej 327, DK-2800 Kgs. Lyngby, Denmark
[9] Institute for Astronomy, Astrophysics, Space Applications and Remote Sensing, National Observatory of Athens, GR-15236 Athens, Greece
[10] Department of Astronomy, Xiamen University, Xiamen, Fujian 361005, People's Republic of China
[11] Purple Mountain Observatory & Key Lab of Radio Astronomy, Chinese Academy of Sciences (CAS), Nanjing 210033, People's Republic of China
[12] Instituto de Astrofísica de Canarias (IAC), E-38205 La Laguna, Tenerife, Spain
[13] Universidad de La Laguna, Dpto. Astrofísica, E-38206 La Laguna, Tenerife, Spain
[14] Center for Extragalactic Astronomy, Durham University, South Road, Durham DH13LE, UK
[15] Research School of Astronomy and Astrophysics, Australian National University, Canberra ACT, 2611, Australia
[16] International Centre for Radio Astronomy Research, University of Western Australia, Crawley, Perth, Western Australia, 6009, Australia
Received 2020 September 29; revised 2020 December 21; accepted 2021 January 1; published 2021 March 4

Abstract

We study the carbon monoxide (CO) excitation, mean molecular gas density, and interstellar radiation field (ISRF) intensity in a comprehensive sample of 76 galaxies from local to high redshift ($z\sim0$–6), selected based on detections of their CO transitions $J=2\rightarrow1$ and $5\rightarrow4$ and their optical/infrared/(sub)millimeter spectral energy distributions (SEDs). We confirm the existence of a tight correlation between CO excitation as traced by the CO (5–4)/(2–1) line ratio R_{52} and the mean ISRF intensity $\langle U\rangle$ as derived from infrared SED fitting using dust SED templates. By modeling the molecular gas density probability distribution function (PDF) in galaxies and predicting CO line ratios with large velocity gradient radiative transfer calculations, we present a framework linking global CO line ratios to the mean molecular hydrogen gas density $\langle n_{\rm H_2}\rangle$ and kinetic temperature $T_{\rm kin}$. Mapping in this way observed R_{52} ratios to $\langle n_{\rm H_2}\rangle$ and $T_{\rm kin}$ probability distributions, we obtain positive $\langle U\rangle$–$\langle n_{\rm H_2}\rangle$ and $\langle U\rangle$–$T_{\rm kin}$ correlations, which imply a scenario in which the ISRF in galaxies is mainly regulated by $T_{\rm kin}$ and (nonlinearly) by $\langle n_{\rm H_2}\rangle$. A small fraction of starburst galaxies showing enhanced $\langle n_{\rm H_2}\rangle$ could be due to merger-driven compaction. Our work demonstrates that ISRF and CO excitation are tightly coupled and that density–PDF modeling is a promising tool for probing detailed ISM properties inside galaxies.

Unified Astronomy Thesaurus concepts: Interstellar medium (847); Star formation (1569); Molecular gas (1073); Starburst galaxies (1570); Spiral galaxies (1560)

1. Introduction

Star formation in galaxies is regulated by their reservoir of molecular gas. Globally, the star formation rate (SFR) correlates with the total amount of molecular gas mass via the Kennicutt–Schmidt law (Schmidt 1959; Kennicutt 1998). Meanwhile, physical properties like density and temperature of the molecular gas also play an important role. For example, observations of different carbon monoxide (CO) rotational transition (J) lines reveal a relatively denser ($n_{\rm H_2}\sim10^{3-4}\,{\rm cm^{-3}}$), highly excited phase of molecular gas in addition to a more diffuse ($n_{\rm H_2}\sim10^{2-3}\,{\rm cm^{-3}}$), less excited phase (e.g., Harris et al. 1991; Wild et al. 1992; Guesten et al. 1993; Mao et al. 2000; Weiß et al. 2001, 2005; Israel & Baas 2002, 2003; Bradford et al. 2003; Bayet et al. 2004, 2006; Israel 2005, 2009a, 2009b; Israel et al. 2006, 2014, 2015; Papadopoulos et al. 2007, 2010a, 2010b, 2012; Kamenetzky et al. 2011, 2012, 2014, 2016, 2017, 2018; Zhang et al. 2014; Liu et al. 2015, hereafter L15; Daddi et al. 2015; Saito et al. 2017), while observations of rotational transition lines of high dipole moment molecules like hydrogen cyanide (HCN) reveal the densest phase of the gas ($n_{\rm H_2}\gtrsim10^{3-4}\,{\rm cm^{-3}}$; e.g., Downes et al. 1992; Brouillet & Schilke 1993; Gao & Solomon 2004a, 2004b; Papadopoulos 2007; Shirley 2015).

In turbulent star formation theory, variations of molecular gas properties are naturally created by turbulence, which is ubiquitous in galaxies (e.g., Nordlund & Padoan 1999; Ostriker et al. 1999; Padoan & Nordlund 2002, 2011; Krumholz & McKee 2005; Krumholz & Thompson 2007; Feldmann et al. 2011; Hennebelle & Chabrier 2011; Padoan et al. 2012; Salim et al. 2015; Leroy et al. 2017; Elmegreen 2018). Turbulence generates certain gas density probability distribution functions (PDFs). At each gas density, CO molecules have different excitation conditions. By solving radiative transfer equations with the large velocity gradient (LVG) assumption (e.g., Goldreich & Kwan 1974), CO line fluxes can be calculated for each given state of gas volume density, column density, CO abundance, LVG velocity gradient, etc. The integrated CO line fluxes from all gas states give the total CO spectral line energy distribution (SLED) as observed. Therefore, CO SLED could be a powerful tracer of turbulence and of molecular gas properties.

Meanwhile, dust grains are also important ingredients of the interstellar medium (ISM), mixed with gas. They are exposed to and heated by the interstellar radiation field (ISRF), and their thermal emission dominates the (far-)infrared/(sub)millimeter part of galaxies' spectral energy distributions (SEDs). Like molecular gas, dust grains do not physically have a single state. Although observational studies sometimes approximate galaxies' dust SEDs by one or two components in modified-blackbody fitting, physical models based on assuming PDFs for the ISRF have been proposed and calculated by Dale et al. (2001), Dale & Helou (2002), Li & Draine (2002), and (Draine & Li 2007, hereafter DL07). See also subsequent applications in Draine et al. (2007, 2014), Aniano et al. (2012, 2020), Magdis et al. (2012), Daddi et al. (2015), Dale et al. (2017), and Schreiber et al. (2018).

Through the study of both CO excitation and dust SED traced mean ISRF intensity ($\langle U \rangle$) in about 20 galaxies, Daddi et al. (2015) found that the CO (5–4)/(2–1) line ratio, R_{52}, is tightly correlated with $\langle U \rangle$. This indicates that CO excitation, or its related ISM properties, is indeed sensitive to the ISRF. However, how the underlying gas density and temperature correlate with ISRF, as well as how this relates to other known correlations like the Kennicutt–Schmidt law, is still unclear.

In this work, we study the CO excitation, molecular gas density, and ISRF in a large sample of 76 (unlensed) galaxies from local to high redshift. The sample is selected from a large compilation of local and high-redshift CO observations from the literature, where we require galaxies to have both CO (2–1) and CO (5–4) detections, together with well-sampled dust SEDs. This also includes CO (5–4) observations newly presented here, from the Institute de Radioastronomie Millimétrique (IRAM) Plateau de Bure Interferometer (PdBI; now upgraded to the NOrthern Extended Millimeter Array [NOEMA]) for six starburst (SB) type galaxies at $z \sim 1.6$ in the COSMOS field, which have Atacama Large Millimeter/Submillimeter Array (ALMA) CO (2–1) from Silverman et al. (2015a).

To estimate gas density and temperature from observed line ratios, we model gas density PDFs following Leroy et al. (2017) but with a new approach incorporating assumptions based on the observed correlations between the gas volume density, column density, and velocity dispersion. We propose a conversion method from the line ratio to the mean molecular hydrogen gas density $\langle n_{\rm H_2} \rangle$ and kinetic temperature $T_{\rm kin}$ for galaxies at global scale.[17] Our model-predicated $J_{\rm u} < 10$ CO SLEDs also show good agreement with the current data.

The structure of this paper is as follows. Section 2 describes the sample and data. Section 3 describes the SED fitting technique for $\langle U \rangle$ and other galaxy properties. In Section 4, we present correlations between R_{52} and various galaxy properties. Then, in Section 5, we describe details of our gas modeling and the conversion from R_{52} to $\langle n_{\rm H_2} \rangle$ and $T_{\rm kin}$, while the resulting correlations between $\langle n_{\rm H_2} \rangle$, $T_{\rm kin}$, and $\langle U \rangle$ are presented in Section 6.2. We discuss the physical meaning of $\langle U \rangle$, the connection from the $\langle U \rangle$–and $T_{\rm kin}$–$\langle n_{\rm H_2} \rangle$ correlations to the Kennicutt–Schmidt law, and the limitations and outlook of our study in Section 6. Finally, we summarize in Section 7.

[17] A PYTHON package (`co-excitation-gas-modeling`) is provided with this paper for the calculation: https://pypi.org/project/co-excitation-gas-modeling. It fits an input line ratio with error to our model grid and determines the probable ranges of $\langle n_{\rm H_2} \rangle$ and $T_{\rm kin}$.

Throughout this paper, line ratios for CO are expressed as flux-to-flux ratio, where fluxes are in units of Jy km s^{-1}. We adopt a flat ΛCDM cosmology with $H_0 = 73$ km s^{-1} Mpc^{-1}, $\Omega_M = 0.27$, and a Chabrier (2003) initial mass function (IMF).

2. Sample and Data

We search the literature for CO observations of local and high-redshift galaxies and seek galaxies that have multiple CO line detections. This is not a complete search, but we have included 132 papers presenting CO observations from 1975 to 2020.[18] We require a galaxy to have one low-J CO line, CO (2–1), and one mid/high-J CO line, CO (5–4), for this work. This approach is chosen to maximize the sample size while covering most high-redshift main-sequence (MS)[19] galaxies' CO observations.

We also require multiwavelength coverage including optical, near-IR, far-infrared, and (sub)millimeter, in order to fit their panchromatic SEDs and obtain stellar and dust properties.

In this way, we build up a sample of 76 galaxies. They are divided into the following subsamples:

1. 22 "local (U)LIRG": local (ultra)luminous infrared galaxies with IR luminosity $L_{\rm IR} \geqslant 10^{11}\,L_\odot$. Their high-$J$ CO data are from the HerCULES (Rosenberg et al. 2015) and GOALS (Armus et al. 2009; Lu et al. 2014, 2015, 2017) surveys using the Spectral and Photometric Imaging Receiver (SPIRE; Griffin et al. 2010) Fourier Transform Spectrometer (FTS; Naylor et al. 2010) on board the Herschel Space Observatory (Pilbratt et al. 2010) and analyzed by L15. Their low-J CO data are from ground-based observations in the literature (see references in Table 1).
2. 16 "local SFG": local star-forming galaxies, most of which have high-J CO from the KINGFISH (Kennicutt et al. 2011) and VNGS (PI: C. Wilson) surveys using Herschel SPIRE FTS, also analyzed by L15. Many of them have low-J CO mapping from the ground-based HERACLES survey (Leroy et al. 2009), while others have CO (2–1) single-pointing observations in the literature.
3. 6 "high-z SB FMOS": redshift $z \sim 1.5$ SB[20] galaxies from the FMOS-COSMOS survey (Silverman et al. 2015b), where CO (2–1) data are from Silverman et al. (2015a) and CO (5–4) data are newly presented in this work.
4. 4 "high-z MS BzK": $z \sim 1.5$ MS galaxies from Daddi et al. (2008, 2010a, 2015), selected using BzK color criterion (Daddi et al. 2004) and representing high-redshift massive star-forming disks.
5. 4 "high-z SB SMG": $z \sim 2$–6 starbursty, (sub)millimeter-selected galaxies, including GN20 (Daddi et al. 2009; Carilli et al. 2010), AzTEC-3 (Riechers et al. 2010), COSBO-11 (Aravena et al. 2008), and HFLS3 (Riechers et al. 2013).

[18] A `MySQL/MariaDB` database is available for interested readers by request.

[19] MS is defined as a sequence between galaxies' stellar mass and star formation rate (SFR) at each redshift (see Noeske et al. 2007; Elbaz et al. 2007; Daddi et al. 2007). In this work we use the Speagle et al. (2014) MS equation.

[20] An SB galaxy is defined by its SFR being 4× greater than the MS SFR (e.g., the Speagle et al. 2014 equation) given its redshift and stellar mass. Vice versa, an MS galaxy is defined by its SFR being within 4× the MS SFR.

Table 1
Sample of Galaxies Used in This Work with Measured and Derived Physical Properties

Source	Subsample	z	R52	$\log\langle n_{\rm H_2}\rangle$	$\langle U\rangle$	$\log L_{\rm IR}$	$\log M_\star$	Reference CO54	Reference CO21
Arp 193	local (U)LIRG	0.023	1.8 ± 0.3	2.4 ± 0.4	$17.0^{+2.4}_{+0.0}$	$11.6^{+0.0}_{-0.0}$	$10.3^{+0.0}_{-0.0}$	L15	P14
Arp 220	local (U)LIRG	0.018	2.4 ± 0.5	2.7 ± 0.7	$20.6^{+0.4}_{-0.1}$	$12.2^{+0.0}_{-0.0}$	$11.0^{+0.0}_{-0.0}$	L15	K14/G09
IRAS F17207–0014	local (U)LIRG	0.043	3.9 ± 1.0	3.5 ± 1.3	$35.0^{+0.2}_{-0.4}$	$12.4^{+0.0}_{-0.0}$	$11.0^{+0.1}_{-0.0}$	L15	K14/B08/W08/P12
IRAS F18293–3413	local (U)LIRG	0.018	2.2 ± 0.1	2.6 ± 0.4	$11.1^{+0.9}_{-2.9}$	$11.7^{+0.0}_{-0.1}$	$9.6^{+0.2}_{-0.2}$	L15	G93
M82	local SFG	0.001	1.7 ± 0.2	2.4 ± 0.3	$25.4^{+0.2}_{-0.5}$	$10.6^{+0.0}_{-0.0}$	$9.8^{+0.0}_{-0.0}$	L15	L09
Mrk 231	local (U)LIRG	0.042	3.0 ± 0.9	2.9 ± 1.3	$50.0^{+0.0}_{-2.5}$	$12.3^{+0.0}_{-0.0}$	$10.9^{+0.0}_{-0.0}$	L15	K14/P12/A07
Mrk 273	local (U)LIRG	0.038	3.4 ± 0.9	3.2 ± 1.3	$37.7^{+5.6}_{+0.0}$	$12.0^{+0.0}_{-0.0}$	$10.6^{+0.0}_{-0.2}$	L15	K14/P12
NGC 0253	local SFG	0.001	2.9 ± 0.7	3.0 ± 1.0	$6.3^{+0.0}_{-0.5}$	$10.6^{+0.0}_{-0.0}$	$10.9^{+0.0}_{-0.1}$	L15	K14(43.5)/H99
NGC 0828	local (U)LIRG	0.018	0.9 ± 0.4	2.1 ± 0.4	$3.5^{+0.5}_{-0.0}$	$11.3^{+0.0}_{-0.0}$	$11.2^{+0.0}_{-0.0}$	L15	P12(22)
NGC 1068	local (U)LIRG	0.004	0.8 ± 0.2	2.1 ± 0.2	$5.8^{+0.2}_{-0.7}$	$11.2^{+0.0}_{-0.0}$	$10.5^{+0.0}_{-0.0}$	L15	K14(43.5)/K11/B08
NGC 1266	local SFG	0.00724	2.6 ± 0.7	2.8 ± 1.0	$13.3^{+3.3}_{-2.0}$	$10.3^{+0.1}_{-0.0}$	$10.5^{+0.0}_{-0.0}$	L15	K14(43.5)/A11/Y11
NGC 1365	local (U)LIRG	0.005	1.5 ± 0.4	2.3 ± 0.5	$3.5^{+0.6}_{-0.0}$	$11.2^{+0.0}_{-0.0}$	$10.9^{+0.0}_{-0.0}$	L15	K14(43.5)/S95
NGC 1614	local (U)LIRG	0.016	1.4 ± 0.3	2.3 ± 0.3	$31.2^{+28.6}_{+0.0}$	$11.6^{+0.1}_{-0.0}$	$10.5^{+0.0}_{-0.2}$	L15	A95(22)
NGC 2369	local (U)LIRG	0.011	2.0 ± 0.4	2.5 ± 0.5	$5.8^{+0.2}_{-1.9}$	$11.1^{+0.0}_{-0.1}$	$10.5^{+0.0}_{-0.0}$	L15	A95(22)/B08
NGC 2623	local (U)LIRG	0.018	4.1 ± 0.8	3.6 ± 1.1	$19.1^{+4.3}_{-2.0}$	$11.4^{+0.0}_{-0.0}$	$10.3^{+0.0}_{-0.0}$	L15	P12/W08
NGC 2798	local SFG	0.00576	1.9 ± 0.3	2.5 ± 0.4	$13.3^{+2.8}_{-2.6}$	$10.5^{+0.0}_{-0.0}$	$9.7^{+0.0}_{-0.0}$	L15	L09
NGC 3256	local (U)LIRG	0.009	1.7 ± 0.2	2.4 ± 0.3	$23.9^{+0.5}_{-9.5}$	$11.6^{+0.0}_{-0.1}$	$10.4^{+0.0}_{-0.0}$	L15	A95(24)/B08/G93
NGC 3351	local SFG	0.0026	0.9 ± 0.2	2.1 ± 0.2	$2.0^{+0.4}_{-0.3}$	$9.8^{+0.0}_{-0.0}$	$9.8^{+0.0}_{-0.0}$	L15	L09
NGC 3627	local SFG	0.00243	1.8 ± 0.4	2.4 ± 0.6	$3.6^{+0.8}_{-1.0}$	$10.3^{+0.0}_{-0.0}$	$10.1^{+0.2}_{-0.0}$	L15	L09
NGC 4321	local SFG	0.00524	0.8 ± 0.1	2.1 ± 0.2	$1.8^{+0.7}_{+0.0}$	$10.4^{+0.0}_{-0.0}$	$10.5^{+0.0}_{-0.0}$	L15	L09
NGC 4536	local SFG	0.00603	1.7 ± 0.3	2.4 ± 0.4	$3.9^{+0.6}_{-0.1}$	$10.3^{+0.0}_{-0.0}$	$10.1^{+0.0}_{-0.0}$	L15	L09
NGC 4569	local SFG	−0.00078	1.1 ± 0.1	2.2 ± 0.2	$1.9^{+0.2}_{-0.3}$	$9.6^{+0.0}_{-0.0}$	$10.5^{+0.0}_{-0.0}$	L15	L09
NGC 4631	local SFG	0.00202	0.9 ± 0.2	2.1 ± 0.3	$2.8^{+0.4}_{-0.6}$	$10.2^{+0.0}_{-0.0}$	$9.4^{+0.0}_{-0.0}$	L15	L09
NGC 4736	local SFG	0.00103	0.6 ± 0.1	2.0 ± 0.1	$4.1^{+1.5}_{-0.4}$	$9.6^{+0.0}_{-0.0}$	$9.8^{+0.0}_{-0.0}$	L15	L09
NGC 4826	local SFG	0.00136	1.6 ± 0.3	2.4 ± 0.4	$3.6^{+0.8}_{-0.6}$	$9.5^{+0.0}_{-0.0}$	$10.4^{+0.0}_{-0.0}$	L15	A95(28)
NGC 4945	local (U)LIRG	0.002	4.0 ± 0.8	3.6 ± 1.2	$7.0^{+0.3}_{-1.0}$	$11.1^{+0.0}_{-0.0}$	$9.7^{+1.1}_{-0.0}$	L15	W04/B08(22)
NGC 5135	local (U)LIRG	0.014	1.6 ± 0.4	2.4 ± 0.4	$8.2^{+2.5}_{-1.2}$	$11.2^{+0.0}_{-0.1}$	$11.1^{+0.0}_{-0.7}$	L15	P12(22)
NGC 5194	local SFG	0.002	0.7 ± 0.1	2.1 ± 0.1	$3.0^{+0.7}_{-0.2}$	$10.2^{+0.0}_{-0.0}$	$9.6^{+0.0}_{-0.0}$	L15	L09
NGC 5713	local SFG	0.00633	1.0 ± 0.2	2.1 ± 0.2	$5.2^{+0.6}_{-1.1}$	$10.4^{+0.0}_{-0.0}$	$10.1^{+0.0}_{-0.0}$	L15	L09
NGC 6240	local (U)LIRG	0.024	2.8 ± 0.8	2.9 ± 0.9	$20.0^{+0.2}_{-0.5}$	$11.7^{+0.0}_{-0.0}$	$10.8^{+0.0}_{-0.0}$	L15	G09
NGC 6946	local SFG	0.00013	1.1 ± 0.1	2.2 ± 0.2	$4.2^{+0.4}_{-1.1}$	$10.4^{+0.0}_{-0.1}$	$10.3^{+0.3}_{-0.0}$	L15	L09
NGC 7469	local (U)LIRG	0.016	1.1 ± 0.3	2.1 ± 0.2	$13.1^{+5.1}_{+0.0}$	$11.6^{+0.0}_{-0.0}$	$10.0^{+0.3}_{-0.0}$	L15	P12
NGC 7552	local (U)LIRG	0.005	2.4 ± 0.5	2.7 ± 0.7	$14.0^{+0.2}_{-0.5}$	$11.1^{+0.0}_{-0.0}$	$10.2^{+0.0}_{-0.0}$	L15	A95
NGC 7582	local SFG	0.005	1.5 ± 0.3	2.3 ± 0.4	$11.7^{+0.2}_{-0.3}$	$10.9^{+0.0}_{-0.0}$	$10.9^{+0.0}_{-0.0}$	L15	A95
MCG +12-02-001	local (U)LIRG	0.016	1.6 ± 0.3	2.3 ± 0.3	$17.4^{+3.6}_{-2.1}$	$11.5^{+0.0}_{-0.0}$	$11.9^{+0.6}_{-1.1}$	L15	K16(43.5)
Mrk 331	local (U)LIRG	0.018	2.4 ± 0.4	2.7 ± 0.7	$14.7^{+0.4}_{-2.1}$	$11.4^{+0.0}_{-0.0}$	$10.9^{+0.0}_{-1.5}$	L15	K16(43.5)
NGC 7771	local (U)LIRG	0.014	1.3 ± 0.2	2.2 ± 0.3	$7.0^{+0.1}_{-0.5}$	$11.3^{+0.0}_{-0.0}$	$11.4^{+0.0}_{-0.0}$	L15	K16(43.5)
IC 1623	local (U)LIRG	0.02	1.8 ± 0.3	2.4 ± 0.5	$13.2^{+0.5}_{-2.1}$	$11.6^{+0.0}_{-0.0}$	$9.1^{+0.0}_{-0.0}$	L15	K16(43.5)
BzK 16000	high-z MS BzK	1.52	1.5 ± 0.3	2.3 ± 0.4	$15.2^{+33.2}_{-13.3}$	$11.8^{+0.0}_{-0.0}$	$11.0^{+0.0}_{-0.2}$	D15	D15/M12
BzK 17999	high-z MS BzK	1.41	2.2 ± 0.2	2.6 ± 0.4	$14.4^{+13.7}_{-7.7}$	$12.0^{+0.0}_{-0.0}$	$10.7^{+0.2}_{-0.0}$	D15	D15/M12
BzK 21000	high-z MS BzK	1.52	2.3 ± 0.2	2.6 ± 0.4	$25.2^{+5.2}_{-12.2}$	$12.3^{+0.0}_{-0.0}$	$11.0^{+0.1}_{-0.2}$	D15	D15/M12
BzK 4171	high-z MS BzK	1.47	1.8 ± 0.2	2.4 ± 0.4	$16.5^{+4.5}_{-8.1}$	$12.0^{+0.0}_{-0.0}$	$10.7^{+0.1}_{-0.1}$	D15	D15/M12
GN 20	high-z SB SMG	4.06	3.4 ± 0.4	3.2 ± 0.7	$35.4^{+4.9}_{-8.8}$	$13.3^{+0.0}_{-0.1}$	$11.2^{+0.0}_{-0.1}$	C10	D09
AzTEC-3	high-z SB SMG	5.3	4.0 ± 0.2	3.6 ± 0.5	$120.2^{+8.9}_{-84.9}$	$13.3^{+0.0}_{-0.1}$	$10.8^{+0.2}_{-0.0}$	R10	R10
COSBO-11	high-z SB SMG	1.83	3.7 ± 0.1	3.3 ± 0.5	$20.0^{+0.4}_{-3.0}$	$12.9^{+0.0}_{-0.0}$	$10.8^{+0.0}_{-0.0}$	A08	A08
HFLS3	high-z SB SMG	6.34	5.9 ± 0.3	5.0 ± 0.4	$68.3^{+10.5}_{-0.0}$	$13.7^{+0.1}_{-0.0}$	$10.5^{+0.5}_{-0.4}$	R13	R13
PACS-819	high-z SB FMOS	1.45	3.5 ± 0.2	3.2 ± 0.5	$27.7^{+5.6}_{-0.1}$	$12.5^{+0.1}_{-0.0}$	$10.7^{+0.1}_{-0.1}$	THIS	S15
PACS-830	high-z SB FMOS	1.46	1.6 ± 0.2	2.4 ± 0.4	$24.3^{+6.7}_{-2.3}$	$12.4^{+0.0}_{-0.0}$	$11.0^{+0.0}_{-0.0}$	THIS	S15
PACS-867	high-z SB FMOS	1.57	1.6 ± 0.3	2.4 ± 0.4	$2.8^{+18.6}_{-2.3}$	$12.0^{+0.0}_{-0.0}$	$10.8^{+0.1}_{-0.1}$	THIS	S15
PACS-299	high-z SB FMOS	1.65	2.6 ± 0.2	2.7 ± 0.4	$28.3^{+38.5}_{-19.1}$	$12.4^{+0.0}_{-0.0}$	$10.1^{+0.4}_{-0.0}$	THIS	S15
PACS-325	high-z SB FMOS	1.65	0.0 ± 3.4	⋯	$1.2^{+14.6}_{-0.7}$	$11.8^{+0.1}_{-0.1}$	$10.4^{+0.0}_{-0.1}$	THIS	S15
PACS-164	high-z SB FMOS	1.65	1.9 ± 0.4	2.4 ± 0.7	$18.1^{+35.0}_{-15.4}$	$12.5^{+0.0}_{-0.0}$	$10.2^{+0.3}_{-0.2}$	THIS	S15
V20-ID41458	high-z SB V20	1.29	1.8 ± 0.2	2.4 ± 0.3	$33.5^{+11.0}_{+0.0}$	$12.5^{+0.0}_{-0.0}$	$11.1^{+0.0}_{-0.0}$	V20	V20
V20-ID21060	high-z SB V20	1.28	3.6 ± 0.9	3.4 ± 1.3	$51.5^{+0.5}_{-1.5}$	$12.3^{+0.0}_{-0.0}$	$10.0^{+0.1}_{-0.0}$	V20	V20
V20-ID51599	high-z SB V20	1.17	2.1 ± 0.2	2.5 ± 0.4	$14.4^{+3.7}_{-1.9}$	$12.5^{+0.0}_{-0.0}$	$11.1^{+0.1}_{-0.0}$	V20	V20
V20-ID30694	high-z MS V20	1.16	1.2 ± 0.2	2.2 ± 0.3	$15.0^{+5.5}_{-2.9}$	$12.0^{+0.1}_{-0.0}$	$10.9^{+0.2}_{-0.0}$	V20	V20
V20-ID38053	high-z SB V20	1.15	1.3 ± 0.4	2.3 ± 0.4	$18.9^{+11.6}_{-0.1}$	$12.0^{+0.0}_{-0.0}$	$10.5^{+0.0}_{-0.0}$	V20	V20
V20-ID48881	high-z SB V20	1.16	1.9 ± 0.5	2.5 ± 0.5	$42.9^{+0.5}_{-0.2}$	$12.3^{+0.0}_{-0.0}$	$10.6^{+0.0}_{-0.0}$	V20	V20

Table 1
(Continued)

Source	Subsample	z	R52	$\log\langle n_{H_2}\rangle$	$\langle U\rangle$	$\log L_{IR}$	$\log M_\star$	Reference CO54	Reference CO21
V20-ID37250	high-z SB V20	1.15	1.1 ± 0.1	2.2 ± 0.2	$9.9^{+3.7}_{-1.1}$	$12.2^{+0.0}_{-0.0}$	$11.0^{+0.0}_{-0.2}$	V20	V20
V20-ID44641	high-z MS V20	1.15	1.0 ± 0.3	2.2 ± 0.5	$9.4^{+2.4}_{-2.8}$	$12.0^{+0.0}_{-0.1}$	$11.2^{+0.0}_{-0.3}$	V20	V20
V20-ID51936	high-z SB V20	1.4	1.9 ± 0.3	2.4 ± 0.3	$5.3^{+2.1}_{-0.1}$	$12.0^{+0.0}_{-0.0}$	$10.5^{+0.0}_{-0.0}$	V20	V20
V20-ID31880	high-z SB V20	1.4	2.2 ± 0.4	2.6 ± 0.5	$20.5^{+2.8}_{+0.0}$	$12.3^{+0.0}_{-0.0}$	$11.0^{+0.0}_{-0.0}$	V20	V20
V20-ID2299	high-z SB V20	1.39	3.4 ± 0.3	3.2 ± 0.5	$13.8^{+0.4}_{-0.4}$	$12.7^{+0.0}_{-0.0}$	$11.1^{+0.0}_{-0.1}$	V20	V20
V20-ID21820	high-z MS V20	1.38	2.1 ± 0.4	2.5 ± 0.5	$15.7^{+7.6}_{-2.3}$	$12.2^{+0.0}_{-0.0}$	$11.0^{+0.0}_{-0.1}$	V20	V20
V20-ID13205	high-z SB V20	1.27	3.0 ± 0.7	3.1 ± 1.2	$49.8^{+16.6}_{-10.8}$	$12.3^{+0.0}_{-0.0}$	$11.1^{+0.0}_{-0.2}$	V20	V20
V20-ID13854	high-z MS V20	1.27	1.8 ± 0.3	2.5 ± 0.5	$20.0^{+0.4}_{-3.0}$	$12.2^{+0.0}_{-0.0}$	$11.1^{+0.0}_{-0.0}$	V20	V20
V20-ID19021	high-z SB V20	1.26	1.9 ± 0.3	2.4 ± 0.4	$25.0^{+5.4}_{+0.0}$	$12.3^{+0.0}_{-0.0}$	$10.4^{+0.0}_{-0.0}$	V20	V20
V20-ID35349	high-z MS V20	1.26	0.8 ± 0.2	2.1 ± 0.2	$8.2^{+4.0}_{-0.6}$	$12.0^{+0.0}_{-0.0}$	$11.2^{+0.0}_{-0.1}$	V20	V20
V20-ID42925	high-z SB V20	1.6	2.1 ± 0.4	2.5 ± 0.5	$59.9^{+0.4}_{-18.5}$	$12.7^{+0.0}_{-0.0}$	$11.0^{+0.0}_{-0.0}$	V20	V20
V20-ID38986	high-z MS V20	1.61	2.8 ± 0.9	2.8 ± 1.4	$19.5^{+155.1}_{-16.1}$	$12.0^{+0.0}_{-0.1}$	$11.1^{+0.0}_{-0.0}$	V20	V20
V20-ID30122	high-z MS V20	1.46	2.0 ± 0.4	2.6 ± 0.6	$13.4^{+1.3}_{-4.2}$	$12.2^{+0.0}_{-0.0}$	$10.9^{+0.1}_{-0.0}$	V20	V20
V20-ID41210	high-z SB V20	1.31	2.1 ± 0.2	2.5 ± 0.4	$25.0^{+0.4}_{-9.6}$	$12.3^{+0.0}_{-0.1}$	$10.6^{+0.0}_{-0.0}$	V20	V20
V20-ID2993	high-z SB V20	1.19	1.4 ± 0.3	2.3 ± 0.4	$13.1^{+7.4}_{-3.0}$	$12.2^{+0.0}_{-0.0}$	$11.0^{+0.1}_{-0.2}$	V20	V20
V20-ID48136	high-z MS V20	1.18	1.5 ± 0.2	2.3 ± 0.3	$14.9^{+3.0}_{-3.3}$	$12.3^{+0.0}_{-0.1}$	$11.1^{+0.1}_{-0.0}$	V20	V20
V20-ID51650	high-z SB V20	1.34	2.8 ± 0.4	2.9 ± 0.6	$21.1^{+9.4}_{-5.0}$	$12.2^{+0.1}_{-0.0}$	$10.9^{+0.0}_{-0.0}$	V20	V20
V20-ID15069	high-z SB V20	1.21	1.7 ± 0.6	2.4 ± 1.0	$6.1^{+2.3}_{-1.2}$	$12.0^{+0.0}_{-0.0}$	$10.8^{+0.1}_{-0.3}$	V20	V20

Note. Only a few selected key columns are shown here. The full sample table has more columns including galaxy properties of DL07 warm- and cold-dust luminosities, AGN luminosities, and offset from the MS, which are used in Figure 2. The full machine-readable table is available at 10.5281/zenodo.3958271.
References THIS = this work (see Appendix A); L15 = Liu et al. (2015); P14 = Papadopoulos et al. (2014); K14 = Kamenetzky et al. (2014); G09 = Greve et al. (2009); E90 = Eckart et al. (1990); I14 = Israel et al. (2014); B08 = Baan et al. (2008); W08 = Wilson et al. (2008); P12 = Papadopoulos et al. (2012); G93 = Garay et al. (1993); L09 = Leroy et al. (2009); B06 = Bayet et al. (2006); A07 = Albrecht et al. (2007); H99 = Harrison et al. (1999); B92 = Braine & Combes (1992); K11 = Kamenetzky et al. (2011); A11 = Alatalo et al. (2011); Y11 = Young et al. (2011); S95 = Sandqvist et al. (1995); A95 = Aalto et al. (1995); W04 = Wang et al. (2004); K16 = Kamenetzky et al. (2016); D15 = Daddi et al. (2015); M12 = Magnelli et al. (2012); D09 = Daddi et al. (2009); W12 = Walter et al. (2012); C10 = Carilli et al. (2010);R10 = Riechers et al. (2010); A08 = Aravena et al. (2008); R13 = Riechers et al. (2013); S15 = Silverman et al. (2015a); V20 = Valentino et al. (2020a).

6. 8 "high-z MS V20": high-redshift MS galaxies from Valentino et al. (2020a), with SFR within 4× the MS SFR.
7. 16 "high-z SB V20": high-redshift SB galaxies from Valentino et al. (2020a), with SFR greater than 4× the MS SFR.

Our sample is shown in Table 1, where references for the CO (2–1) and CO (5–4) observations are provided. We note that there are also additional interesting galaxies observed in these CO lines: for example, strongly lensed galaxies (e.g., Yang et al. 2017; Harrington et al. 2018), or galaxies that have observations of different CO lines (e.g., Boogaard et al. 2019). As the sample we compiled in this work already covers a large variety of galaxy types (e.g., MS/SB, local/high-redshift), we chose not to further include these data for simplicity and consistency. Applying our method to an extended sample of galaxies could be the subject of a future study.

In the following, we present more details about the CO and multiwavelength photometry data for subsamples.

2.1. Local (U)LIRGs and SFGs

For local galaxies, all high-J ($J_u \sim 4$–13) CO observations are taken with Herschel SPIRE FTS. L15 explored the full public Herschel Science Archive and reduced the spectra for almost all (167) FTS-observed local galaxies.[21] Based on their sample, we select galaxies with CO (5–4) S/N > 3 and cross-match them with low-J ($J_u \sim 1$ and 2) observations in the literature (i.e., 132 papers). There are about 40 galaxies that meet our criterion.

The FTS's spatial pixel ("spaxel") has a beam size of about 20″–40″ across its frequency range of 447–1568 GHz. As we attempt to recover the total flux from the finite beam size as reliably as possible, a few interacting galaxies (e.g., NGC 4038/39; Arp 299 A/B/C) and very nearby, large galaxies (e.g., Cen A, NGC 891, M83) have been excluded. This gives us a sample of 38 galaxies with both CO (2–1) and CO (5–4) detections, of which 22 are local (U)LIRGs whose CO (5–4) transitions were mainly observed by the HerCULES and GOALS surveys, while ground-based CO (2–1) was provided by various works in the literature (see Table 1). Meanwhile, 16 are local star-forming spiral galaxies, whose CO (5–4) data are mostly taken by the KINGFISH and VNGS surveys, and 12 of which have CO (2–1) mapping from the HERACLES survey (Leroy et al. 2009).[22]

We provide some notes about galaxies that have multiple, possibly inconsistent CO measurements in the literature in Appendix B. In some cases these early observations do not fully agree with each other, even after accounting for the effect of different beam sizes. This could be due to absolute flux calibration or single-dish baseline issues. Thus, it is likely that the uncertainty in these CO fluxes could be quite high, e.g., a factor of two.

To correct for the fact that FTS spaxel beam sizes are smaller than entire galaxies, L15 measured the Herschel PACS 70–160 μm

[21] Their catalog is available at https://zenodo.org/record/3632388.

[22] Their data are available at http://www.mpia.de/HERACLES/Overview.html.

aperture photometries within each FTS CO line beam size, as well as for the entire galaxy, and calculated the ratio between the beam-aperture photometry and the entire galaxy photometry, namely, "BeamFrac," as listed in the full Table 1 (online version). This BeamFrac is then used to scale the measured CO line flux in the FTS central spaxel to the entire galaxy scale. This method is based on the assumption that PACS 70–160 μm luminosity linearly traces CO (5–4) luminosity and is also adopted by other works, e.g., Kamenetzky et al. (2014, 2016, 2017) and Lu et al. (2017).

For nearby galaxies that have CO (2–1) maps from HERACLES, we measure their CO (2–1) integrated fluxes using our own photometry method, as some of them do not have published line fluxes in Leroy et al. (2009). Because the signal-to-noise ratio is relatively poor when reaching galaxies' outer disks in the HERACLES data, aperture photometry can be strongly affected by the choice of aperture size. We thus perform a signal masking of the HERACLES moment-0 maps to distinguish pure noise pixels from signal pixels. The mask is iteratively generated, median filtered, and binary dilated based on pixels above 1σ, where σ is the rms noise iteratively determined on the pixels outside the signal mask. In this way, we obtain a Gaussian-distributed pixel value histogram outside the mask and a total CO (2–1) line flux from the sum of pixels within the mask. We compared our CO (2–1) line fluxes with those published in Leroy et al. (2009) for available galaxies, finding relative differences to be as small as 5%–10%.

To study the dust SED and ISRF of these galaxies, we further collected multiwavelength photometry data in the literature. In our sample, 22, 15, 7, and 6 galaxies have Herschel far-IR photometry from Chu et al. (2017), Dale et al. (2017), Clark et al. (2018), and Clements et al. (2018), respectively. Eight have SCUBA2 850 μm photometry from Lisenfeld et al. (2000). Note that Dale et al. (2017) provide the full UV/optical-to-infrared/submillimeter SEDs.[23] All of these local galaxies have Herschel PACS 70 or 100 μm and 160 μm photometry from L15. Fluxes are consistent among these works. For example, comparing L15 with Chu et al. (2017), we find 13 galaxies in common, and their median flux ratio in logarithm is −0.01 dex, with a scatter of 0.04 dex. For our SED fitting, we average all available fluxes for each band.

In addition, we cross-matched with Brown et al. (2014), Jarrett et al. (2003), Brauher et al. (2008), and the NASA Extragalactic Database (NED) for missing optical to near-/mid-infrared photometry. All local galaxies have Two Micron All Sky Survey near-IR photometry from Jarrett et al. (2003) except for NGC 2369 and NGC 3256. For nine galaxies that do not have any optical photometry from Dale et al. (2017) and Brown et al. (2014), we use the optical/near-IR/mid-IR photometry from NED.[24]

2.2. High-z SB FMOS Galaxies with New PdBI Observations

We observed the CO (5–4) line emission in six $z\sim1.6$ SB galaxies from the FMOS-COSMOS survey (Silverman et al. 2015b) with IRAM PdBI in the winter of 2014 (program ID W14DS). These galaxies have ALMA CO (2–1) observations presented in Silverman et al. (2015a). Our PdBI observations are at 1.3 mm. Phase centers are set to the ALMA CO (2–1) emission peak position for each galaxy, and the on-source integration time is 1.5–3.1 hr per source. Sensitivity is 0.6–0.7 mJy beam^{-1} over the expected line widths of 200–600 MHz, depending on the ALMA CO (2–1) line properties of each source. With robust weighting (robust factor 1), the cleaned images have synthesized beam FWHM of 2.″0–3.″3.

As the ALMA CO (2–1) data have much higher S/N than the PdBI CO (5–4) data, we extract the CO (5–4) line fluxes in the *u-v* plane by Gaussian source fitting with fixed CO (2–1) positions and line widths (from Silverman et al. 2015a), using the GILDAS[25] `MAPPING UV_FIT` task. The achieved line flux S/Ns are 1.8–5.4 within the subsample. For two sources, PACS-819 and PACS-830, which are spatially resolved in ALMA CO (2–1) data, we also fix their CO (5–4) sizes to the measured CO (2–1) sizes (∼0.″3–1.″0, respectively) in the `UV_FIT` fitting, so as to account for the fact that they are marginally resolved in the PdBI data. For other galaxies with smaller ALMA CO (2–1) sizes, we consider them unresolved by the PdBI beam.

Furthermore, we partially observed their CO (1–0) line emission with the Very Large Array (VLA; project code 17A-233). The observing program is incomplete, and none have full integration (PACS-867, PACS-299, and PACS-164 each have about 90 minutes of on-source integration), but we provide face-value measurements obtained as for CO (2–1). We list the new CO (5–4) and CO (1–0) line fluxes and upper limits, together with the Silverman et al. (2015a) CO (2–1) line fluxes, in Table 2 in Appendix A.

Multiwavelength photometry is available from Laigle et al. (2016) and Jin et al. (2018), thanks to the rich observational data in the COSMOS deep field (see also McCracken et al. 2012; Ilbert et al. 2013; Muzzin et al. 2013; Liu et al. 2019a).

2.3. High-z MS BzK Galaxies

We include four *BzK* color-selected MS galaxies from Daddi et al. (2015) in our sample. They represent typical high-redshift star-forming MS galaxies and are consistent with having a disk-like morphology. Their CO (5–4) observations were taken with IRAM PdBI in 2009 and 2011 by Daddi et al. (2015), and CO (2–1) in 2007–2009 by Daddi et al. (2010a).

These galaxies have optical to near-IR photometry from Skelton et al. (2014) and far-IR to (sub)millimeter and radio photometry from Liu et al. (2018) based on the Herschel PEP (Lutz et al. 2011), HerMES (Roseboom et al. 2010), and GOODS-Herschel surveys (Elbaz et al. 2011) and ground-based SCUBA2 S2CLS (Geach et al. 2017) and AzTEC +MAMBO surveys (Greve et al. 2008; Perera et al. 2008; Penner et al. 2011).

Daddi et al. (2015) presented a similar panchromatic SED fitting to that in this work with the full DL07 dust models (see Section 3) to estimate ISRF $\langle U\rangle$ and other SED properties, but without including an active galactic nucleus (AGN) component in the modeling. Our SED fitting allows for the inclusion of a mid-IR AGN component, but we confirm that such an AGN component is not required, based on the chi-square statistics.

[23] Including Galaxy Evolution Explorer (GALEX) far-UV, near-UV, *B*, *V*, *R*, *I*, *u*, *g*, *r*, *i*, *z*, *J*, *H*, *K*, Spitzer/IRAC 3.6, 4.5, 5.8, 8.0 μm, Wide-field Infrared Survey Explorer 12 μm, Spitzer/MIPS 24 μm, Herschel/PACS 70, 100, 160 μm, Herschel/SPIRE 250, 350, 500 μm, and JCMT/SCUBA 850 μm. See their Table 2.

[24] These are Mrk 231, NGC 0253, NGC 1365, NGC 2369, NGC 3256, NGC 4945, NGC 5135, NGC 7469, and NGC 7582. Note that we carefully selected photometric data with large-enough aperture to cover entire galaxies.

[25] http://gildas.iram.fr

Thus, we obtain similar results in terms of $\langle U \rangle$ to those of Daddi et al. (2015).

2.4. High-z SB SMGs

We include four submillimeter-selected high-redshift galaxies in our study: GN20 (Daddi et al. 2009; Carilli et al. 2010; Tan et al. 2014), AzTEC-3 (Riechers et al. 2010), COSBO-11 (Aravena et al. 2008), and HFLS3 (Riechers et al. 2013; Cooray et al. 2014; Laporte et al. 2015). Due to their submillimeter selection, they usually have very high SFRs compared to MS galaxies with similar stellar masses; therefore, we consider them as SBs. We note that there are now more than 100 submillimeter-selected high-redshift ($z \gtrsim 1$) galaxies that have CO detections, but only a few tens have both CO (5–4) and (2–1) detections. We further excluded strongly lensed galaxies lacking optical/near-IR SEDs, for example, those from Cox et al. (2011), Yang et al. (2017), Bothwell et al. (2017), Cañameras et al. (2018), and Harrington et al. (2018, 2019), despite the fairly good sampling of their CO SLEDs. Their strong magnification ($\gtrsim$10) largely reduces the observing time ($\times 1/100$) for CO observations compared to unlensed targets, yet their optical to mid-IR SEDs are usually not well sampled. Harrington et al. (2021) present a study of CO excitation and far-IR/(sub)millimeter dust SED modeling in strongly lensed galaxies, based on a similar gas density PDF modeling.

Among our SMG subsample, GN20 is in the GOODS-North field, and AzTEC-3 and COSBO-11 are in the COSMOS field. They have rich multiwavelength photometry as mentioned earlier. Tan et al. (2014) fitted the GN20 SED with DL07 templates without an AGN component, and our new fitting to the same photometry data shows that a mid-IR AGN component is indistinguishable from the warm dust component in the DL07 models. The inclusion of the AGN component in this work, however, leads to more realistic uncertainties in the derived $\langle U \rangle$ parameter.

2.5. High-z MS and SB Galaxies from V20

We further include 8 MS and 16 SB galaxies from Valentino et al. (2020a) that have both CO (2–1) and CO (5–4) S/N > 3 detections and far-IR photometric data. Valentino et al. (2018, 2020a, 2020b) surveyed 123, 75, and 15 galaxies with ALMA through Cycles 3, 4, and 7, respectively. Cycle 3 and 4 observations targeted CO (5–4) and CO (2–1), respectively. Their sample is selected from the COSMOS field at $z \approx 1.1$–1.7 based on predicted CO line luminosities, which are further based on the CO–IR luminosity correlation (Daddi et al. 2015). By this selection, this sample contains both MS and SB galaxies. We divide MS and SB galaxies into two subsamples for illustration in the later sections.

These galaxies have multiwavelength photometry similarly to the other COSMOS galaxies mentioned above, and most of them also have one or more ALMA dust continuum measurements from the public ALMA archive, reduced by Liu et al. (2019a, 2019b), and from line-free channels of CO observations in Valentino et al. (2020a). Valentino et al. (2020a) did multicomponent SED fitting including stellar, AGN, and DL07 warm- and cold-dust components following Magdis et al. (2012, 2017). They adopt a slightly different definition of ISRF, $\langle U \rangle_{\rm V20} = 1/125 \times L_{\rm IR}/M_{\rm dust}$, where their $L_{\rm IR}$ also includes the AGN contribution. In this work, we assembled all available ALMA photometry and refitted their SEDs with our own code. To be consistent within this work, we still use the $\langle U \rangle$ definition according to DL07 (their Equation (33)) and use only the star-forming dust components without the contribution of AGN torus. Because of the different definition and treatment of the AGN component, there are some noticeable differences in $\langle U \rangle$ between Valentino et al. (2020a) and our study. However, if we were to adopt the same $\langle U \rangle_{\rm V20}$ definition, the $\langle U \rangle$ derivations would become fully consistent.

3. SED Fitting: The MICHI2 Code

The well-sampled SEDs from optical to far-IR/millimeter allow us to obtain accurate dust properties by fitting them with SED templates. Particularly, since dust grains do not have a single temperature in a galaxy, the mean ISRF intensity, $\langle U \rangle$, has been considered to be a more physical proxy of dust emission properties (DL07). It represents the 0–13.6 eV intensity of interstellar UV radiation in units of the Mathis et al. (1983) ISRF intensity (see Draine et al. 2007).

The $\langle U \rangle$ parameter has advantages in describing mixture states of ISRF over using a single or several dust temperature values to describe galaxy dust SEDs. In DL07 dust models, the majority of dust grains are exposed to a minimum ambient ISRF with intensity $U_{\rm min}$, while the rest are exposed to the photon-dominated region (PDR) ISRF, with intensities ranging from $U_{\rm min}$ to $U_{\rm max}$ in a power-law PDF (in mass). The mass fraction of the latter dust grain population ("warm dust" or "PDR dust") is expressed as $f_{\rm PDR}$ in this work and is a free parameter in the fit. $U_{\rm min}$ is another free parameter, while $U_{\rm max}$ is empirically fixed, as well as the power-law index (see more detailed introduction in Draine et al. 2007, 2014; Aniano et al. 2012, 2020). As pointed out by Dale & Helou (2002), such a physically driven dust model actually fits the mass distribution of molecular clouds (Stutzki 2001; Shirley et al. 2002; Elmegreen 2002). Based on this model, DL07 generated SED templates that can then be used for fitting by other works using their own SED fitting code.

In this work, we use our own-developed SED fitting code, MICHI2,[26] providing us the flexibility in combining multiple SED components and choosing SED templates for each component. Comparing with popular panchromatic (UV-to-millimeter/radio) SED fitting codes, e.g., `MAGPHYS` (da Cunha et al. 2008, 2015), `LePhare` (Arnouts et al. 1999; Ilbert et al. 2006), and `CIGALE` (Noll et al. 2009; Ciesla et al. 2015; Boquien et al. 2019), our code fits SEDs well and produces similar best-fitting results (see Appendix C). Our code also performs χ^2-based posterior probability distribution analysis and estimates reasonable (asymmetric) uncertainties for each free or derived parameter (e.g., Figure 1).

Our code can also handle an arbitrary number of SED libraries as the components of the whole SED. For example, we use five SED libraries/components representing stellar, AGN, DL07 warm dust, DL07 cold dust, and radio emissions (see below). Our code samples their combinations in the five-dimensional space, then generates a composite SED (after multiplying the model with the filter curves), and then fits to the observed photometric data and obtains χ^2 statistics. The post-processing of the χ^2 distribution provides the best-fit and probability range of each physical parameter in the SED libraries (following Press et al. 1992, chapter 15.6).

[26] https://github.com/1054/Crab.Toolkit.michi2

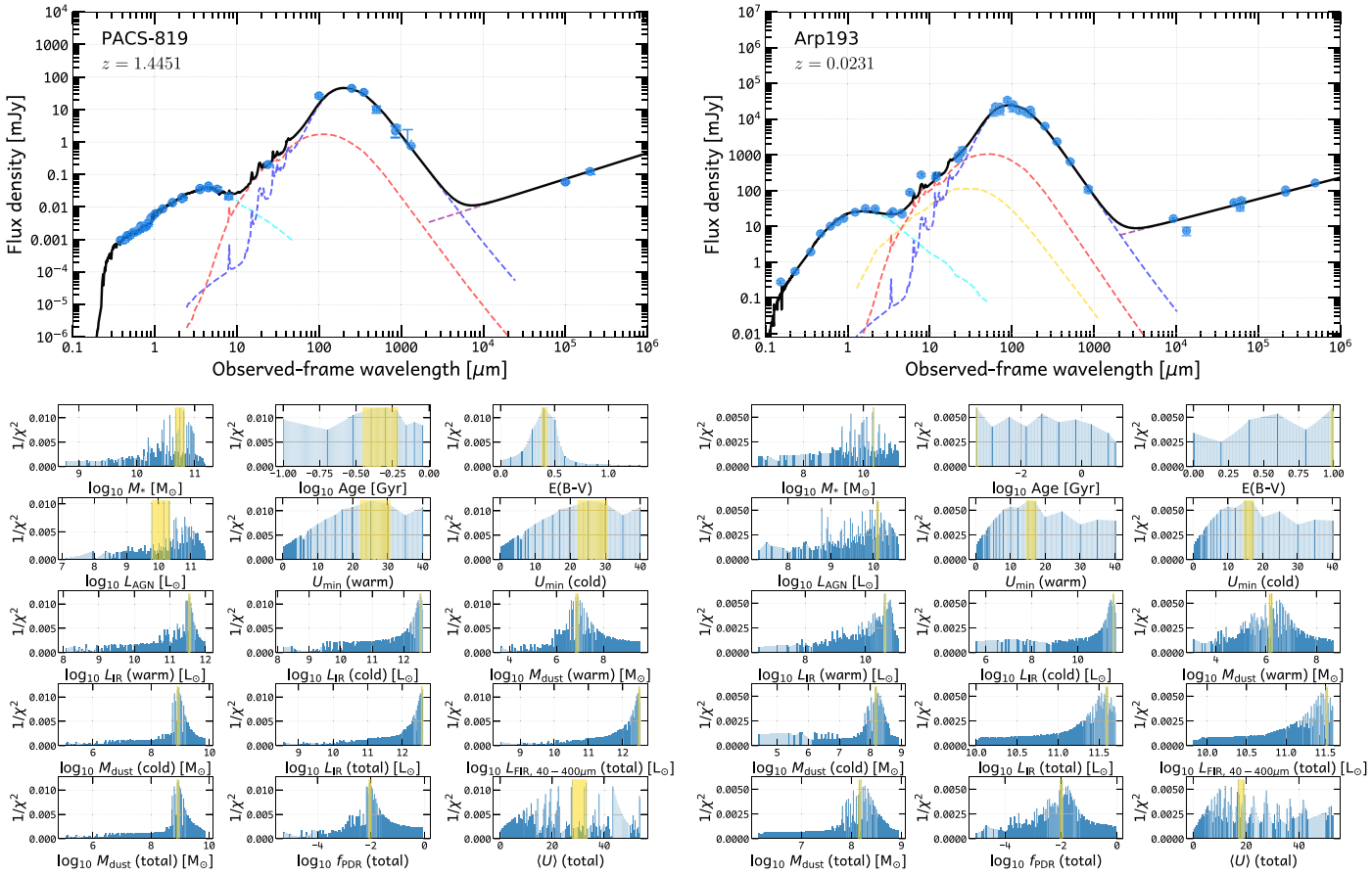

Figure 1. Two examples of our SED fitting for PACS-819 (left) and Arp 193 (right) with our MICHI2 code as described in Section 3. Upper panels show the best-fit SED (black line) and SED components, which are stellar (cyan dashed line), mid-IR AGN (yellow dashed line, optional if AGN is present), PDR dust (red dashed line), and cold/ambient dust (blue dashed line). Photometry data are shown by circles with error bars or downward-pointing arrows for upper limits if S/N < 3. Lower panels show $1/\chi^2$ distributions for several galaxy properties from our SED fitting. In each subpanel, the height of the histogram indicates the highest $1/\chi^2$ in each bin of the x-axis galaxy property. A higher $1/\chi^2$ means a better fit. The 68% confidence level for our five SED component fitting is indicated by the yellow shading. (Figures for all sources are available at 10.5281/zenodo.3958271).

Details of the five SED libraries/components are as follows:

1. Stellar component: for high-redshift ($z > 1$) SFGs, we use the Bruzual & Charlot (2003) code to generate solar metallicity, constant star formation history (SFH), and Chabrier (2003) IMF SED templates and then apply the Calzetti et al. (2000) attenuation law with a range of $E(B-V) = 0.0-1.0$ to construct our SED library. For local galaxies, we use the FSPS (Conroy et al. 2009; Conroy & Gunn 2010a, 2010b) code to generate solar -metallicity, τ-declining SFH, Chabrier (2003) IMF SED templates (also with the Calzetti et al. 2000 attenuation law), as this generates a larger variety of SED templates that fit local galaxies better.
2. Mid-IR AGN component: we use the observationally calibrated AGN torus SED templates from Mullaney et al. (2011). They cover 6–100 μm in wavelengths and can fit type 1, type 2, and intermediate-type AGNs as demonstrated by Mullaney et al. (2011).
3. DL07 warm dust component for dust grains exposed to the PDR ISRF with intensity ranging from U_{min} to $U_{max} = 10^7$ in a power-law PDF with an index of -2 (updated version; see Draine et al. 2014; Aniano et al. 2020). The fraction of dust mass in polycyclic aromatic hydrocarbons (PAHs) is described by q_{PAH}. The contribution of such warm dust to total ISM dust in mass is described by f_{PDR} in this work (i.e., the γ in DL07). Free parameters are U_{min}, q_{PAH}, and f_{PDR}.
4. DL07 cold-dust component for dust grains exposed to the ambient ISRF with intensity of U_{min}. The U_{min} and q_{PAH} of the cold dust are fixed to be the same as the warm dust in our fitting.
5. Radio component: a simple power-law with index -0.8 is assumed. Our code has the option to fix the normalization of the radio component at rest-frame 1.4 GHz to the total IR luminosity $L_{IR(8-1000\ \mu m)}$ (integrating warm- and cold-dust components only) via assumptions about the IR $-$radio correlation (e.g., Condon et al. 1991; Yun et al. 2001; Ivison et al. 2010; Magnelli et al. 2015) when galaxies lack sufficient IR photometric data and display no obvious radio excess due to AGNs (e.g., Liu et al. 2018). As radio is not the focus of this work, we only use the simple power-law assumption for illustration purposes.

Note that we do not balance the dust-attenuated stellar light with the total dust emission. This has the advantage of allowing for optically thick dust emission that is only seen in the infrared. Our fitting then outputs χ^2 distributions for the following parameters of interest (see bottom panels in Figure 1):

1. Stellar properties, including stellar mass $M_\star$, dust attenuation $E(B-V)$, and light-weighted stellar age.
2. AGN luminosity $L_{\rm AGN}$, integrated over the AGN SED component.
3. IR luminosities for cold dust ($L_{\rm IR,cold\ dust}$), warm dust ($L_{\rm IR,PDR\ dust}$) and their sum ($L_{\rm IR,total\ dust}$).
4. Mean ISRF intensity $\langle U\rangle$, minimum ISRF intensity $U_{\rm min}$, and the mass fraction of warm/PDR-like dust in the DL07 model $f_{\rm PDR}$.

In Figure 1 we show two examples of our SED fitting. Best-fit parameters and their errors are also listed in our full sample table (Table 1 online version).

To verify our SED fitting, we also fit our high-z galaxies' SEDs with MAGPHYS and CIGALE (see more details in Appendix C). We find that for most high-z galaxies the stellar masses and IR luminosities agree within ∼0.2–0.3 dex. The IR luminosities are more consistent than stellar masses among the results of three fitting codes, with a scatter of ∼0.2 dex. In several outlier cases, our code produces more reasonable fitting to the data (e.g., AzTEC-3, Arp220, NGC 0253), which is likely because we do not have an energy balance constraint in the code. Our code has no systematic bias against CIGALE, but there is a noticeable trend that MAGPHYS fits slightly larger stellar masses than the other two. A possible reason is the use of the Charlot & Fall (2000) double attenuation law in MAGPHYS (see Lo Faro et al. 2017) rather than the Calzetti et al. (2000) attenuation law in our MICHI2 and CIGALE fitting.

Given the general agreement between our code and CIGALE/MAGPHYS, and to be consistent within this paper, we fit all SEDs with our MICHI2 SED fitting code with the five SED libraries as mentioned above.

4. ISRF Traces CO Excitation: The $\langle U\rangle$–R_{52} Correlation

We use our SED fitting results and the compiled CO data to study the empirical correlation between the CO (5–4)/CO (2–1) line ratio R_{52} and the mean ISRF intensity $\langle U\rangle$. This correlation physically links molecular gas and dust properties together, supporting the idea that gas and dust are generally mixed together at large scales and exposed to the same local ISRF.

In Figure 2 we correlate R_{52} with various galaxy properties derived from our SED fitting. Panel (a) shows a tight correlation between R_{52} and the ambient ISRF intensity $U_{\rm min}$, and panel (b) confirms the tight correlation between R_{52} and $\langle U\rangle$ that was first reported by Daddi et al. (2015). Panels (c) and (d) show that CO excitation is also well correlated with galaxies' dust luminosities, but not with their stellar masses. In panels (e)−(g), we show that R_{52} exhibits no correlation with $f_{\rm PDR}$ and mid-IR AGN fraction, while a very weak correlation seems to exist between R_{52} and the offset to the MS SFR, SFR/SFR$_{\rm MS}$. In each panel, the Pearson correlation coefficient P is computed and shown in the lower right corner. These correlations, or lack thereof, demonstrate that R_{52} or mid-J CO excitation is indeed mostly driven by dust-related quantities, i.e., $L_{\rm IR}$, $\langle U\rangle$, and $U_{\rm min}$.

Our best-fitting R_{52}–$\langle U\rangle$ correlation is close to the one found by Daddi et al. (2015), yet somewhat shallower than that. Valentino et al. (2020a) also reported a shallower slope of the R_{52}–$\langle U\rangle$ correlation, given that the high-z V20 sample is used in both their and this work. Indeed, subsamples behave slightly differently in Figure 2. While local SFGs and local (U)LIRGs are scattered well around the average R_{52}–$\langle U\rangle$ correlation line, high-z MS and SB galaxies from the FMOS and V20 subsamples tend to lie below it. Given the varied S/N of IR data as reflected by the $\langle U\rangle$ error bars, the majority of those high-z galaxies do not have a high-quality constraint on $\langle U\rangle$. High-z sample selections for CO observations are usually also biased to high-z IR-bright galaxies. Therefore, it is difficult to draw a conclusion about any redshift evolution of the R_{52}–$\langle U\rangle$ correlation with the current data set.

From panel (f) of Figure 2, we can see that there are several galaxies showing a high AGN-to-ISM dust luminosity ratio (note that the AGN luminosity is integrated over all wavelengths, while the IR luminosity is only DL07 warm +cold dust integrated over 8–1000 μm). The three galaxies with $L_{\rm AGN,all\lambda}/L_{\rm IR,8-1000\mu m}\gtrsim 0.9$ are V20-ID38986, V20-ID51936, and V20-ID19021, from high to low, respectively. They all clearly show power-law shape SEDs from the near-IR IRAC bands to mid-IR MIPS 24 μm and PACS 100 μm.[27] However, their R_{52} do not tend to be higher. This likely supports that these mid-J ($J_{\rm u}\sim 5$) CO lines are not overwhelmingly affected by AGNs.

We note that the correlations in Figure 2 are not the only ones worth exploring. R_{52} also correlates with dust mass in a way similar to $\langle U\rangle$ but with larger scatter, and $\langle U\rangle$ can be considered as the ratio of $L_{\rm IR}/M_{\rm dust}$; therefore, here we omit the correlation with $M_{\rm dust}$. Daddi et al. (2015) also investigated how SFR surface density ($\Sigma_{\rm SFR}$), star formation efficiency (SFR/$M_{\rm gas}$), gas-to-dust ratio ($\delta_{\rm GDR}$), and massive star-forming clumps affect $\langle U\rangle$ and R_{52}. Their results support the idea that a larger fraction of massive star-forming clumps with denser molecular gas compared to the diffuse, low-density molecular gas is the key for a high CO excitation (as proposed by the simulation work of Bournaud et al. 2015). Therefore, to understand the key physical drivers of CO excitation, information on molecular gas density distributions is likely the most urgently required.

5. Modeling of Molecular Gas Density Distribution in Galaxies

CO line emission in galaxies arises mainly from the cold molecular gas, and CO line ratios/SLEDs are sensitive to local molecular gas physical conditions, i.e., volume density $n_{\rm H_2}$, column density $N_{\rm H_2}$, and kinetic temperature $T_{\rm kin}$. These properties typically vary by one to three orders of magnitude within a galaxy, e.g., as seen in observations as reviewed by Young & Scoville (1991), Solomon & Vanden Bout (2005), Carilli & Walter (2013), and Combes (2018) and references therein, and also in modeling and simulations, e.g., by Krumholz & Thompson (2007), Glover & Clark (2012), Smith et al. (2014b), Narayanan & Krumholz (2014), Bournaud et al. (2015), Glover et al. (2015), Glover & Smith (2016), Popping et al. (2016, 2019), Renaud et al. (2019b, 2019a), and Tress et al. (2020).

In practice, studies of the CO SLED at a global galaxy scale or at subkiloparsec scales usually require the presence of a relatively dense gas component ($n_{\rm H_2}\sim 10^{3-5}\,{\rm cm^{-3}}$; $T_{\rm kin}\gtrsim$ 50–100 K) in addition to a relatively diffuse gas ($n_{\rm H_2}\sim 10^{2-3}\,{\rm cm^{-3}}$;

[27] Their SED figures are accessible at the link mentioned in the caption of Figure 1. With high-S/N IRAC to MIPS 24 μm data, their mid-IR AGNs and any PAH feature if present can be well distinguished by our SED fitting. Yet we note that for galaxies with low-S/N IRAC to MIPS 24 μm data the uncertainty in AGN component identification could be high.

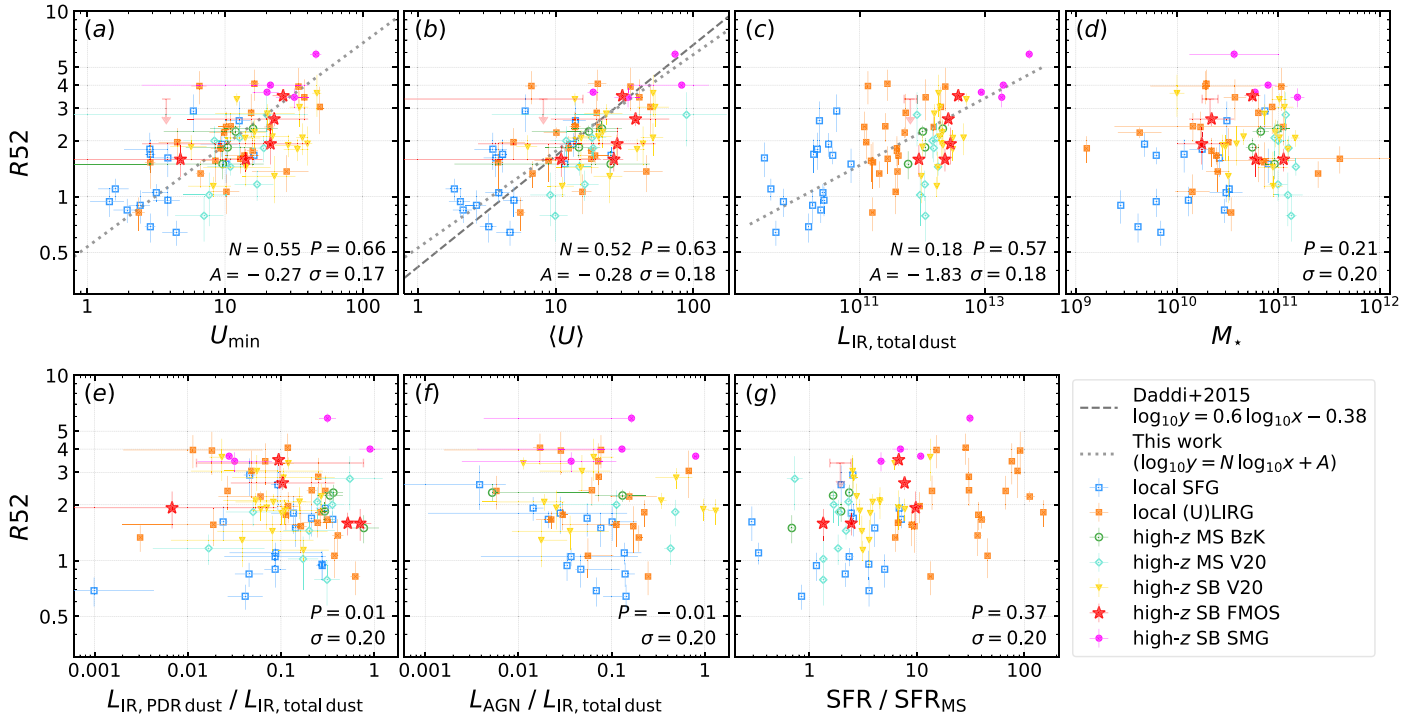

Figure 2. CO (5–4) to(2–1) line ratio R_{52} vs. various galaxy properties: (a) ambient ISRF intensity (U_{min}); (b) mean ISRF intensity ($\langle U \rangle$); (c) dust IR luminosity; (d) stellar mass; (e) luminosity fraction of dust exposed to warm/PDR-like ISRF to total dust in ISM (does not include AGN torus); (f) luminosity ratio between mid-IR AGN and total ISM dust (AGN luminosity is integrated over for all available wavelengths, while dust luminosity is integrated over rest-frame 8–1000 μm); and (g) the offset to the MS in terms of SFR. The Pearson coefficient P and scatter σ for each correlation are shown in the lower right corner. We performed orthogonal distance regression (ODR) linear regression fitting to the data points and their x and y errors in panels (a)–(c), where $P > 0.5$. Dotted lines are the best fits from this work, with slope N and intercept A shown at the bottom. The dashed line in panel (b) is the best-fit linear regression from Daddi et al. (2015).

$T_{kin} \sim 20$–100 K), via non-local thermodynamic equilibrium (non-LTE) LVG radiative transfer modeling (e.g., Israel et al. 1995; Mao et al. 2000; Israel & Baas 2001, 2002, 2003; Weiß et al. 2001, 2005; Bradford et al. 2003; Zhu et al. 2003; Bayet et al. 2004, 2006, 2009; Papadopoulos et al. 2007, 2008, 2010a, 2010b, 2012; Hailey-Dunsheath et al. 2008, 2012; Panuzzo et al. 2010; Rangwala et al. 2011; Papadopoulos et al. 2012; Spinoglio et al. 2012; Meijerink et al. 2013; Pereira-Santaella et al. 2013; Rigopoulou et al. 2013; Greve et al. 2014; Kamenetzky et al. 2014, 2016, 2017; Lu et al. 2014, 2017; Rosenberg et al. 2014a, 2014b; Schirm et al. 2014, 2017; Zhang et al. 2014; Israel et al. 2015; Liu et al. 2015; Mashian et al. 2015; Wu et al. 2015; Yang et al. 2017; Valentino et al. 2020a). A third state that is mostly responsible for $J_u \gtrsim 10$ CO lines is also found in the case of AGNs (e.g., van der Werf et al. 2010; Rangwala et al. 2011; Spinoglio et al. 2012) or mechanical heating (e.g., Rosenberg et al. 2014a). Therefore, a mid-J-to-low-J CO line ratio like R_{52} reflects not only the excitation condition of a single gas state but also the relative amount of the denser and warmer to the more diffuse gas component.

Leroy et al. (2017) have conducted pioneer modeling of the sub-beam gas density PDF to understand line ratios of CO isotopologue and dense gas tracers. The method includes constructing a series of one-zone clouds, performing non-LTE LVG calculation, and compositing line fluxes by the gas density PDF. They demonstrated that such modeling can successfully reproduce observed isotopologue or dense gas tracers to CO line ratios. Inspired by this work, we present in this section similar sub-beam density–PDF gas modeling to study the CO excitation and propose a useful conversion from R_{52} observations to $\langle n_{H_2} \rangle$ and T_{kin} for galaxies at global scales.

5.1. Observational Evidences of Gas Density PDF

Observation of gas density PDF at molecular cloud scale requires high angular resolution (e.g., sub-hundred-parsec scales) and full spatial information; therefore, it could only be obtained either with sensitive single-dish mapping in the Galaxy and nearest large galaxies or with sensitive interferometric plus total power observations. For external galaxies, the MAGMA survey by Pineda et al. (2009), Hughes et al. (2010), and Wong et al. (2011) mapped CO (1–0) in the LMC at 11 pc resolution with the Mopra 22 m single-dish telescope. Gardan et al. (2007), Gratier et al. (2010), and Druard et al. (2014) mapped M33 CO (2–1) emission at 50 pc scale with the IRAM 30 m single-dish telescope. The PAWS survey provides M51 CO maps at 40 pc obtained with the IRAM PdBI and with IRAM 30 m data (Hughes et al. 2013; Pety et al. 2013; Schinnerer et al. 2013; Leroy et al. 2016; Schinnerer et al. 2017). The ongoing PHANGS-ALMA survey[28] maps CO (2–1) at ~60–100 pc scales in more than 70 nearby galaxies using ALMA with total power (A. Leroy et al. 2021, in preparation; see also Kreckel et al. 2018; Sun et al. 2018, 2020; Schinnerer et al. 2019; Chevance et al. 2020). Meanwhile, higher physical resolution observations are also available for Galactic clouds and filaments, e.g., Kainulainen & Tan (2013), Lombardi et al. (2014, 2015), Kainulainen & Federrath (2017), and Zhang et al. (2019), to name a few.

These observations at large scales reveal a smooth gas density PDF that can be described by a lognormal distribution plus a high-density power-law tail (e.g., Wong et al. 2011; Hughes et al. 2013;

[28] http://phangs.org

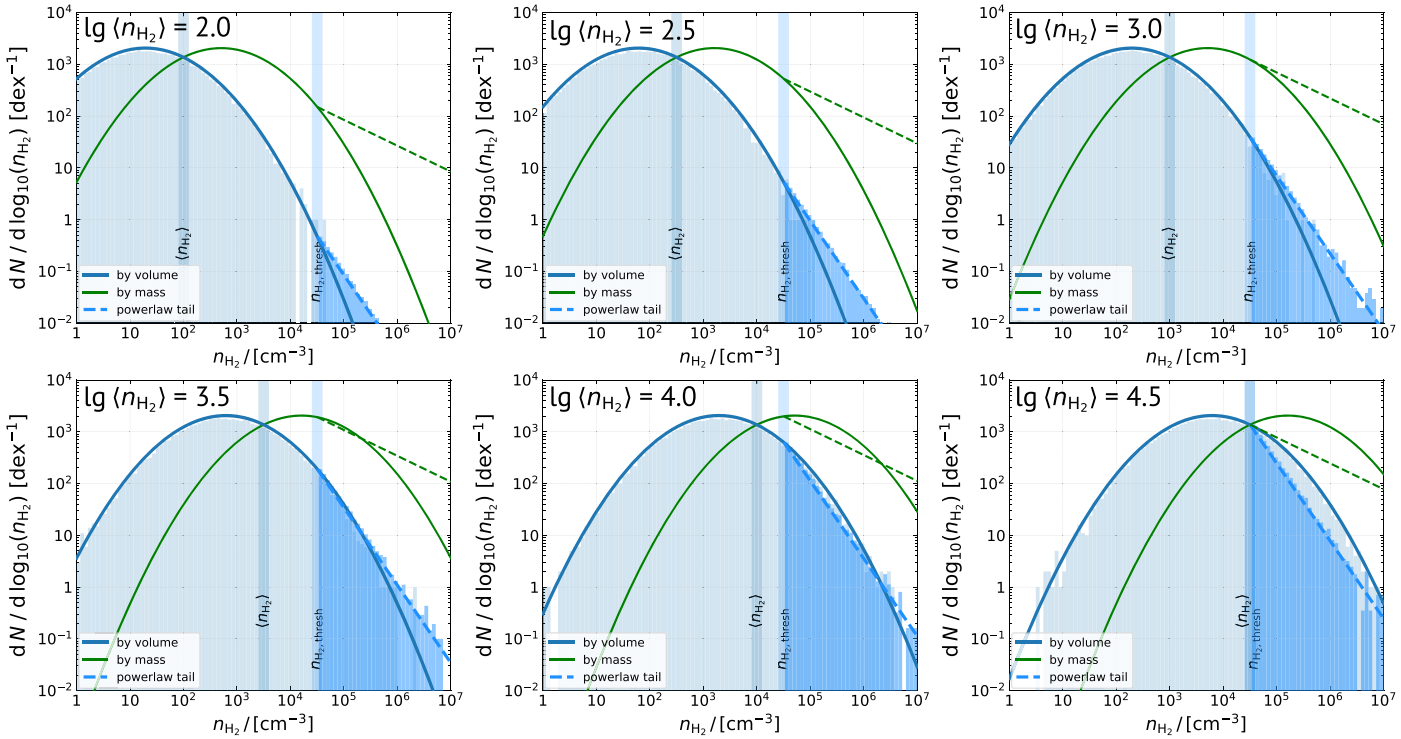

Figure 3. Example of composite gas density PDFs in our modeling with varied lognormal PDFs mean gas density $\log_{10}\langle n_{H_2}\rangle$ (from 2.0 to 4.5 in panels from left to right and top to bottom) and a fixed power-law tail threshold gas density $\log_{10}(n_{H_2,\mathrm{thresh}}) = 4.5$. The $\log_{10}\langle n_{H_2}\rangle$ and $\log_{10}(n_{H_2,\mathrm{thresh}}) = 4.5$ are indicated by the vertical transparent bars and labels in each panel. The thick blue and thin green solid (dashed) lines represent the volume- and mass-weighted PDFs of the lognormal (power-law tail) gas component, respectively.

Druard et al. 2014). The width of the lognormal PDF and the slope of the power-law tail do slightly vary among galaxies, but the most prominent difference is seen for the mean of the lognormal PDF (hereafter $\langle n_{H_2}\rangle$), which changes by more than one order of magnitude (for a relatively small sample of <10 spiral galaxies; see Figure 7 of Leroy et al. 2016).

Interestingly, such a lognormal PDF is consistently predicted by isothermal homogeneous supersonic turbulent theories or diverse cloud models (e.g., Ostriker et al. 2001; Vázquez-Semadeni & García 2001; Padoan & Nordlund 2002; Padoan et al. 2004a, 2004b; Tassis et al. 2010; Padoan & Nordlund 2011; Padoan et al. 2012; Kritsuk et al. 2017; Raskutti et al. 2017; see also references in Raskutti et al. 2017), and the additional power-law PDF is also expected, e.g., for a multiphase ISM and/or due to the cloud evolution/star formation at late times (e.g., Klessen et al. 2000; Tassis et al. 2010; Kritsuk et al. 2017; Raskutti et al. 2017 and references therein). Therefore, modeling gas density PDFs assuming a lognormal distribution plus a power-law tail appears to be a very reasonable approach.

5.2. Sub-beam Gas Density PDF Modeling

We thus assume that the line-of-sight volume density of molecular gas in a galaxy follows a lognormal PDF, with a small portion of lines of sight following a power-law PDF at the high-density tail. Representative PDFs are shown in Figure 3. Each PDF samples the n_{H_2} from 1 to $10^7\,\mathrm{cm}^{-3}$ in 100 bins in logarithmic space. For each n_{H_2} bin, the height of the PDF is thus proportional to the number of sight lines with a density of n_{H_2}. We assume that the CO line emission surface brightness from each line of sight can be computed from an equivalent "one-zone" cloud with a single n_{H_2}, N_{H_2}, T_{kin}, velocity gradient, and CO abundance. Thus, the total CO line emission surface brightness is the sum of all sight lines in the PDF.

The shape of the gas density PDF is described by the following parameters: the mean gas density of the lognormal PDF $\langle n_{H_2}\rangle$, the threshold density of the power-law tail $n_{H_2,\mathrm{thresh}}$, the width of the lognormal PDF, and the slope of the power-law tail. We model a series of PDFs by varying the $\langle n_{H_2}\rangle$ from $10^{2.0}$ to $10^{5.0}\,\mathrm{cm}^{-3}$ in steps of 0.25 dex and $n_{H_2,\mathrm{thresh}}$ from $10^{4.0}$ to $10^{5.25}\,\mathrm{cm}^{-3}$ in steps of 0.25 dex, to build our model grid, which can cover most situations observed in galaxies. The slope of the power-law tail is fixed to -1.5, which is an intermediate value as indicated by simulations (Federrath & Klessen 2013), also previously adopted by Leroy et al. (2017). The width of the lognormal PDF is physically characterized by the Mach number of the supersonic turbulent ISM (see Padoan & Nordlund 2002, 2011 and Equation (5) of Leroy et al. 2017): $\sigma \approx 0.43\sqrt{\ln(1 + 0.25\mathcal{M}^2)}$, which ranges typically from 4 to 20 in star-forming regions as shown by simulations (e.g., Krumholz & McKee 2005; Padoan & Nordlund 2011). Here we adopt a fiducial Mach number of 10, as done previously by Leroy et al. (2017). Note that a high Mach number of ∼80 is also found in merger systems and SB galaxies (e.g., Leroy et al. 2016). It corresponds to a lognormal PDF width 1.56× our fiducial value and marginally affects the CO excitation in a similar way to a higher $\langle n_{H_2}\rangle$. Thus, for simplicity in this work we fix the Mach number and allow $\langle n_{H_2}\rangle$ to vary.

5.3. One-zone Gas Cloud Calculation

For a given gas density PDF, each n_{H_2} bin is composed of the same "one-zone" gas clouds for which we will compute the line

surface brightness. A one-zone cloud has a single volume density $n_{\rm H_2}$, column density $N_{\rm H_2}$, gas kinetic temperature ($T_{\rm kin}$), CO abundance [CO/H$_2$], and velocity gradient dv/dr. Note that although an equivalent cloud size r is implied from the ratio of $N_{\rm H_2}$ and $n_{\rm H_2}$, given that the calculation is in 1D, r should not be taken as a physical cloud size. Also note that in our study we do not model the 3D distribution of one-zone models; therefore, any radiative coupling between one-zone models along the same line of sight cannot be accounted for. This is likely a minor issue for star-forming disk galaxies given their thin disks (a few hundred parsecs; Wilson et al. 2019) and systematic rotation that separates molecular clouds in the velocity space for inclined disks, but the actual effects need to be studied by detailed numerical simulations (e.g., Smith et al. 2020; Tress et al. 2020).

Here we use RADEX (van der Tak et al. 2007) to compute the 1D non-LTE radiative transfer. For a given $n_{\rm H_2}$, we loop $N_{\rm H_2}$ from 10^{21} to 10^{24} cm^{-2}, and r is then determined by

$$N_{\rm H_2} = 2 \times r \times n_{\rm H_2} = 6 \times 10^{18} \times \frac{r}{\rm pc} \times \frac{n_{\rm H_2}}{\rm cm^{-3}} \ \ ({\rm cm^{-2}}). \tag{1}$$

We also loop over $T_{\rm kin}$ values of 25, 50, and 100 K, while we fix $[{\rm CO/H_2}] = 5 \times 10^{-5}$, a reasonable guess for star-forming clouds (e.g., Leung & Liszt 1976; van Dishoeck & Black 1987, 1988), although it varies from cloud to cloud and depends on chemistry (e.g., Sheffer et al. 2008). Note that there is one additional free parameter to set, i.e., the LVG velocity gradient dv/dr, or the line width FWHM ΔV, or the velocity dispersion σ_V. They are related to each other by

$$\begin{aligned} \Delta V &= 2 \times r \times dv/dr \ \ ({\rm km\ s^{-1}}) \\ \sigma_V &= \Delta V/(2\sqrt{2\ln 2}) \ \ ({\rm km\ s^{-1}}). \end{aligned} \tag{2}$$

To determine these quantities and effectively reduce the number of free parameters while being consistent with observations, we use an empirical correlation between $N_{\rm H_2}$, r, σ_V, and the virial parameter $\alpha_{\rm vir}$. $\alpha_{\rm vir}$ describes the ratio of a cloud's kinetic energy and gravitational potential energy (e.g., Bertoldi & McKee 1992) and can be written as $\frac{5\sigma_V^2 r}{fGM}$, where σ_V and r are introduced above, G is the gravitational constant, M is the cloud mass, and f is a factor to account for the lack of balance between kinetic and gravitational potential (see Equation (6) of Sun et al. 2018). Observations show that clouds are not always virialized, i.e., $\alpha_{\rm vir}$ is not always unity. Based on ~60 pc CO mapping of 11 galaxies in the PHANGS-ALMA sample, Sun et al. (2018) reported the following correlation in their Equation (13) (helium and other heavy elements are included; see also Equation (2) in the review by Heyer & Dame 2015):

$$\begin{aligned} \alpha_{\rm vir} &= 5.77 \times \left(\frac{\sigma_V}{\rm km\ s^{-1}}\right)^2 \left(\frac{\Sigma_{\rm H_2}}{\rm M_\odot\ pc^{-2}}\right)^{-1} \left(\frac{r}{\rm 40\ pc}\right)^{-1} \\ &= 5.77 \times \left(\frac{\sigma_V}{\rm km\ s^{-1}}\right)^2 \left(\frac{N_{\rm H_2}}{\rm 1.55 \times 10^{20}\ cm^{-2}}\right)^{-1} \left(\frac{r}{\rm pc}\right)^{-1}. \end{aligned} \tag{3}$$

They find $\alpha_{\rm vir} \approx 1.5$–$3.0$ with a 1σ width of 0.4–0.65 dex. For simplicity and also with the idea of focusing primarily on the effect of gas density, we adopt a constant $\alpha_{\rm vir}$ of 2.3. As shown in later sections, this is already sufficient to explain the observed CO line ratios/SLEDs by our modeling. But note that more comprehensive descriptions of $\alpha_{\rm vir}$ can be achieved in simulations and can be compared with the results from this work to better understand how a changing $\alpha_{\rm vir}$ could affect CO line ratio prediction.

Figure 4 presents how R_{52} changes with the gas densities of one-zone cloud models for four representative redshifts where the cosmic microwave background (CMB) temperatures are different. We repeat our calculations for three representative $T_{\rm kin}$ as labeled in each panel. The comparison shows that $T_{\rm kin}$ significantly affects the R_{52} line ratio, especially at low densities and at low redshifts. Note that due to the constant $\alpha_{\rm vir}$ assumption, for a given $n_{\rm H_2}$, Equation (3) implies that $\sigma_V \propto r$ and that dv/dr is not varying with $N_{\rm H_2}$. Thus, the actual choices of $N_{\rm H_2}$ (or r) for each single one-zone model will not affect the modeling of R_{52} (and of the optical depth τ).

In addition, our modeling is also able to produce reasonable line optical depths (τ) and [C I]/CO line ratios, as presented in Appendix D.

5.4. Converting R_{52} to $\langle n_{\rm H_2}\rangle$ and T_{kin} with the Model Grid

We compute the global line surface brightness by summing one-zone line surface brightnesses at each $n_{\rm H_2}$ bin according to the gas density PDF. With our assumptions, there are only four free parameters: the mean gas density of the lognormal PDF $\langle n_{\rm H_2}\rangle$, the threshold density of the power-law tail $n_{\rm H_2,thresh}$, gas kinetic temperature $T_{\rm kin}$, and redshift. Their grids are described in Section 5.2.

In Figure 5, we present the predicted R_{52} as a function of the four free parameters. R_{52} increases smoothly with $\langle n_{\rm H_2}\rangle$ and $T_{\rm kin}$, while $n_{\rm H_2,thresh}$ does not substantially alter the R_{52} ratio, as indicated by the color-coding. The minimum R_{52} at the lowest density ($\log_{10}\langle n_{\rm H_2}\rangle/{\rm cm^{-3}} \sim 2$) is nearly doubled from redshift 0 to 6 owing to the increasing CMB temperature, but such a redshift effect is less prominent ($<\times 1.5$) both at higher density ($\log_{10}\langle n_{\rm H_2}\rangle/{\rm cm^{-3}} > 3$) and for higher $T_{\rm kin}$.

In Figure 6, we further show the full CO SLEDs at $J_{\rm u} = 1$–9 from our model grid and compare them with a subsample of galaxies with multiple CO transitions at various redshifts. These galaxies are displayed in panels where the $\langle n_{\rm H_2}\rangle$ is closest to their R_{52}-derived $\langle n_{\rm H_2}\rangle$ (see below). Our modeling can generally match these CO SLEDs given certain choices of $\langle n_{\rm H_2}\rangle$ and $T_{\rm kin}$. Yet we caution that this is not a thorough comparison, and our model grid might not fit entirely well the CO SLED shape owing to our simplifying assumptions of fixed Mach number and power-law tail slope or $\alpha_{\rm vir}$. While this work only focuses on R_{52} with the simplest assumptions, the model predictions seem overall already quite promising for the whole CO SLEDs and can be further improved in future works.

Based on the model grid, we describe below a method to determine the most probable $\langle n_{\rm H_2}\rangle$, $T_{\rm kin}$, and $n_{\rm H_2,thresh}$ ranges for a given R_{52} and its error in galaxies with known redshift. This is done with a Monte Carlo approach. We first interpolate our 4D model grid to the exact redshift of each galaxy using PYTHON `scipy.interpolate.LinearNDInterpolator` and then resample the 3D model grid to a finer grid, perturb the R_{52} given its error over a normal distribution for 300 realizations, and find the minimum χ^2 best fits for each realization. Finally, we combine best fits to obtain posterior distributions of $\langle n_{\rm H_2}\rangle$, $T_{\rm kin}$, and $n_{\rm H_2,thresh}$ and determine their median, 16th percentile (L68), and 84th percentile

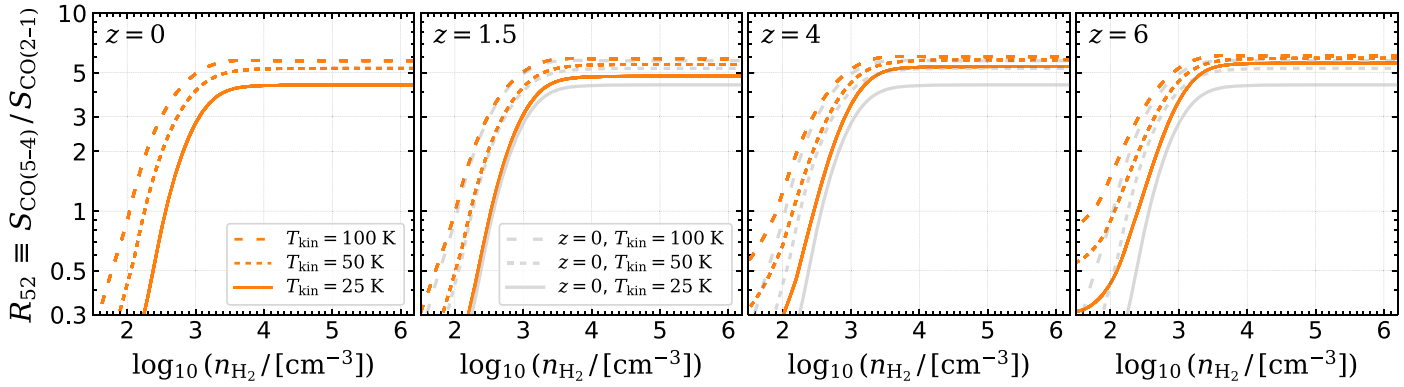

Figure 4. CO (5–4)/CO (2–1) line ratio (R_{52}) from single one-zone LVG calculation. The four panels show the calculations at four representative redshifts $z = 0$, 1.5, 4, and 6, from left to right, respectively. Solid, dashed, and long-dashed lines are for gas kinetic temperature $T_{kin} = 25$, 50, and 100 K, respectively. The gray lines in the second, third, and fourth panels are the corresponding $z = 0$ lines.

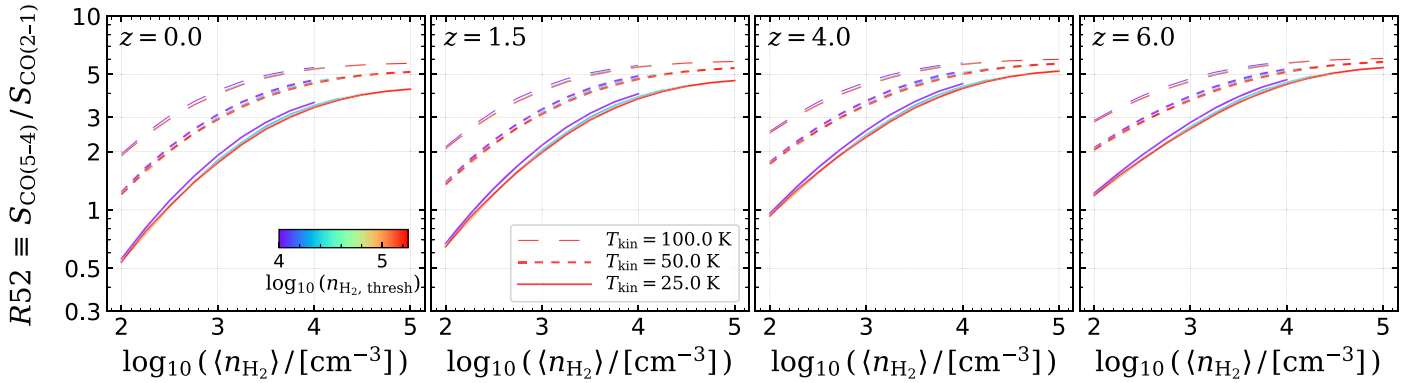

Figure 5. R_{52} as functions of the mean gas density ($\log_{10}\langle n_{H_2}\rangle$) as predicted from our composite gas modeling. The four panels show the models at four different representative redshifts. In each panel, color indicates the threshold density of the power-law tail ($\log_{10}(n_{H_2,thresh})$; which alters the line ratio only slightly), and three line styles are models at three representative kinetic temperatures ($T_{kin} = 25$, 50, and 100 K for solid, dashed, and long-dashed lines, respectively).

(H68). This fitting method is coded in our PYTHON package `co-excitation-gas-modeling` that is made publicly available.

We note that although there is a single input observation (R_{52}) whereas there are three parameters to be determined ($\langle n_{H_2}\rangle$, T_{kin}, and $n_{H_2,thresh}$), our method still produces reasonable results. In fact, our method is able to take into account the internal degeneracy between $\langle n_{H_2}\rangle$ and T_{kin} inside model grids, thus obtaining reasonable probability ranges. Figure 7 shows the fitted $\langle n_{H_2}\rangle$ and T_{kin} for our galaxy sample, resulting in a nonlinear trend between $\langle n_{H_2}\rangle$ and T_{kin}. The galaxy-wide mean pressures of gas can also be calculated as $T_{kin} \times \langle n_{H_2}\rangle$ and are found to agree with estimates in local galaxies (Kamenetzky et al. 2014).

In Figures 8 and 9, we present correlations between the R_{52}-fitted $\langle n_{H_2}\rangle$ and T_{kin}, respectively, and various galaxy properties, similarly to what is presented in Figure 2 for R_{52}. We discuss them in detail in the next sections (Section 6.2).

6. Results on ISM Physical Properties and Discussion

6.1. The Underlying Meaning of $\langle U\rangle$: A Mass-to-light Ratio for Dust

By definition, $\langle U\rangle$ is the mass-weighted ISRF intensity created by UV photons from stars in a galaxy. As indicated by the DL07 model and many of its applications, e.g., Draine et al. (2007, 2014), Aniano et al. (2012, 2020), Dale et al. (2012, 2017), Magdis et al. (2012, 2017), Ciesla et al. (2014) and Schreiber et al. (2018), $\langle U\rangle$ is actually a mass-weighted, average mass-to-light ratio for the mixture of dust grains in a galaxy. It is driven by the young stars emitting most of the UV photons, but it also reflects the mean distance between young stars and interstellar dust and the efficiency of UV photons heating the dust. For a given DL07 ISRF distribution power-law index (=−2) and U_{max} (=10^7; Draine et al. 2014), $\langle U\rangle$ is proportional to the ratio between L_{IR} and M_{dust}, with a coefficient $P_0 \approx 138$ from this work, where P_0 represents the power absorbed per unit dust mass in a radiation field $U = 1$:

$$L_{IR,8-1000\mu m} = P_0 \cdot \langle U\rangle \cdot M_{dust}$$
$$\text{where } P_0 \approx 120\text{–}150 \text{ (mean} = 138). \quad (4)$$

Note that the P_0 factor is calibrated to be equal to 125 in Magdis et al. (2012) owing to a slightly different $U_{max} = 10^6$, a small 10% systematic difference.

$\langle U\rangle$ is also positively linked to dust temperature, but it depends on how dust temperature is defined. For example, Draine et al. (2007) find that $T \approx 17 \cdot U^{1/6}$ (K) for dust grains with sizes greater than 0.03 μm whose blackbody radiation peaks around 160 μm. Schreiber et al. (2018) calibrate the light-weighted dust temperature $T_{dust}^{light} = 20.0 \cdot U^{1/5.57}$ (K) (and mass-weighted $T_{dust}^{mass} = 0.91 \cdot T_{dust}^{light}$) by fitting Wien's law to each elementary Galliano et al. (2011) template.

Studies of T_{dust} and $\langle U\rangle$ have shown that dust (ISRF) is warmer (stronger) for increasing IR luminosity from local SFGs to (U)LIRGs (e.g., Hwang et al. 2010; Symeonidis et al. 2013; Herrero-Illana et al. 2019) and increases with redshift for the majority of MS galaxies (e.g., Magdis et al. 2012; Magnelli et al. 2014; Béthermin et al. 2015; Schreiber et al. 2018). Some observations show colder dust temperatures in a few among the

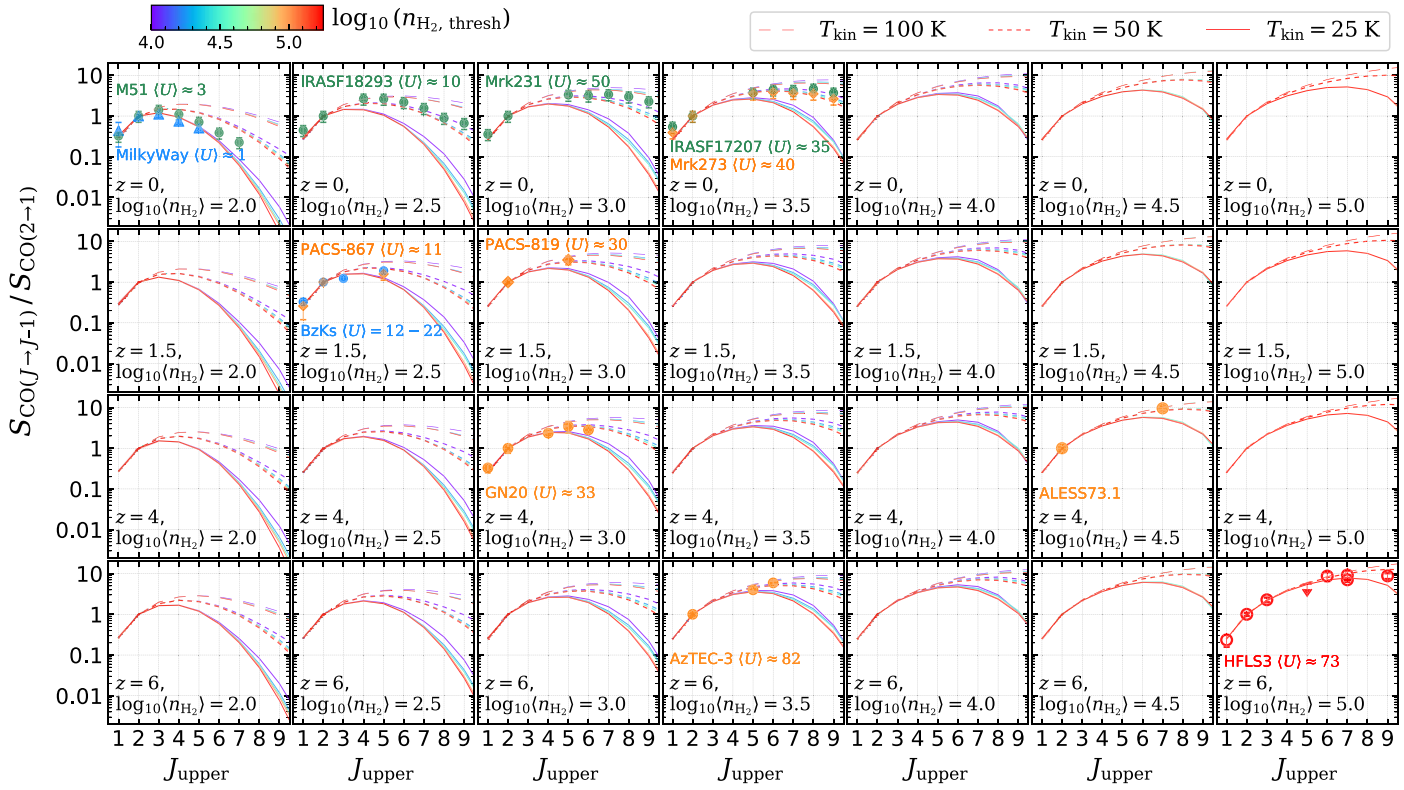

Figure 6. Predicted CO SLEDs in Jansky units and normalized at CO (2–1). From top to bottom, CO SLEDs are at redshift $z = 0$, 1.5, 4, and 6, respectively. And from left to right, lognormal PDFs mean gas density $\log_{10}\langle n_{H_2}\rangle/\mathrm{cm}^{-3}$ changes from 2.0 to 5.0 in steps of 0.5. In each panel, solid, dashed, and long-dashed lines represent $T_{kin} = 25$, 50, and 100 K models, respectively. Line color-coding indicates the threshold gas density of the power-law tail PDF, $\log_{10}(n_{H_2,thresh})$. Colored data points are CO line fluxes in the following galaxies, with references in parentheses: the Milky Way (Fixsen et al. 1999), local spiral M51 (Schirm et al. 2017), local ULIRGs Mrk 231, IRAS F18293–3413, and IRAS F17207–0014 (L15, Kamenetzky et al. 2014), $z = 1.5$ BzK galaxies (Daddi et al. 2015), $z = 1.5$ starburst galaxies (Silverman et al. 2015b and this work). $z = 4.055$ SMG GN20 (Daddi et al. 2009; Carilli et al. 2010; Tan et al. 2014), $z = 4.755$ SMG ALESS73.1 (Coppin et al. 2010; Zhao et al. 2020), $z = 5.3$ SMG AzTEC-3 (Riechers et al. 2010), and $z = 6.3$ SMG HFLS3 (Riechers et al. 2013).

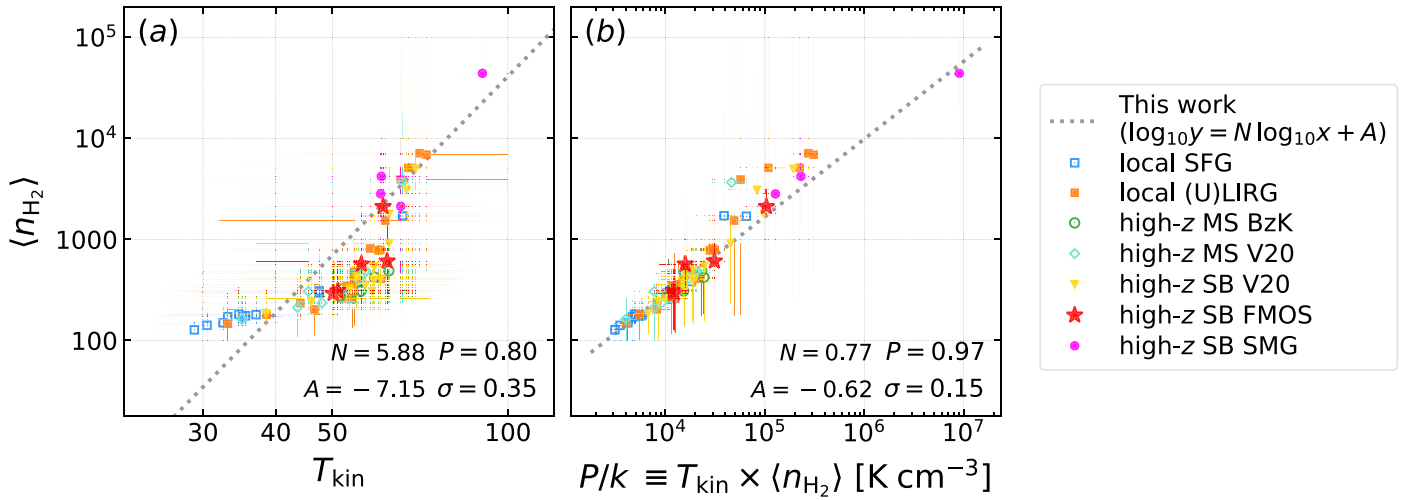

Figure 7. Fitted mean gas density $\langle n_{H_2}\rangle$ vs. fitted gas kinetic temperature T_{kin} (left panel) and gas pressure P/k (right panel; k is the Boltzmann constant) based on R_{52} and its errors in our galaxy sample. This reflects the internal degeneracy between $\langle n_{H_2}\rangle$ and T_{kin} in our model grid. See fitting method in Section 5.4.

most extreme SB systems (e.g., Lisenfeld et al. 2000; Jin et al. 2019; Cortzen et al. 2020). These are likely due to the presence of high dust opacity at shorter wavelengths, which makes the dust SED apparently colder. Observations of SMGs also show colder dust temperatures in some of the less luminous ones. This phenomenon is likely driven by the fact that (sub)millimeter selection favors cold-dust galaxies whose SEDs peak closer to (sub)millimeter wavelengths (e.g., Chapman et al. 2005; Kovács et al. 2006; Symeonidis et al. 2009, 2011; Hwang et al. 2010; Magdis et al. 2010; Magnelli et al. 2010).

There is also an interesting finding that for extreme SB galaxies with $\mathrm{SFR}/\mathrm{SFR}_{MS} > 4$ their $\langle U\rangle$ seem to not evolve with redshift (e.g., Béthermin et al. 2015), while $\langle U\rangle$ in MS galaxies does evolve with redshift, and extrapolation. This suggests that $\langle U\rangle$ in MS galaxies might become stronger than those in extreme SB galaxies at $z > 2.5$, which seems at odds with the expectation.

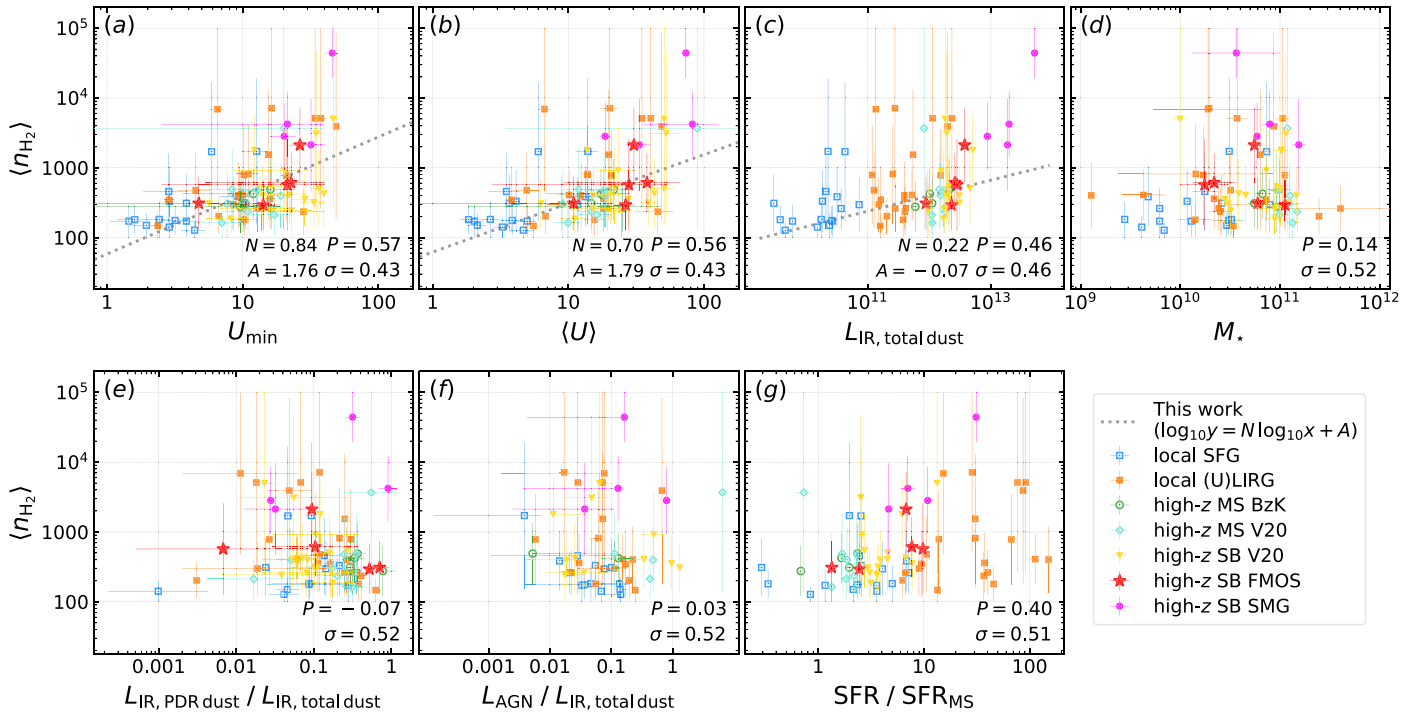

Figure 8. Fitted n_{H_2} vs. galaxy properties, as in Figure 2. Data points' n_{H_2} and error bars are the median and 1σ ranges of the fitting using our model grid as presented in Section 5 to the observed R_{52}.

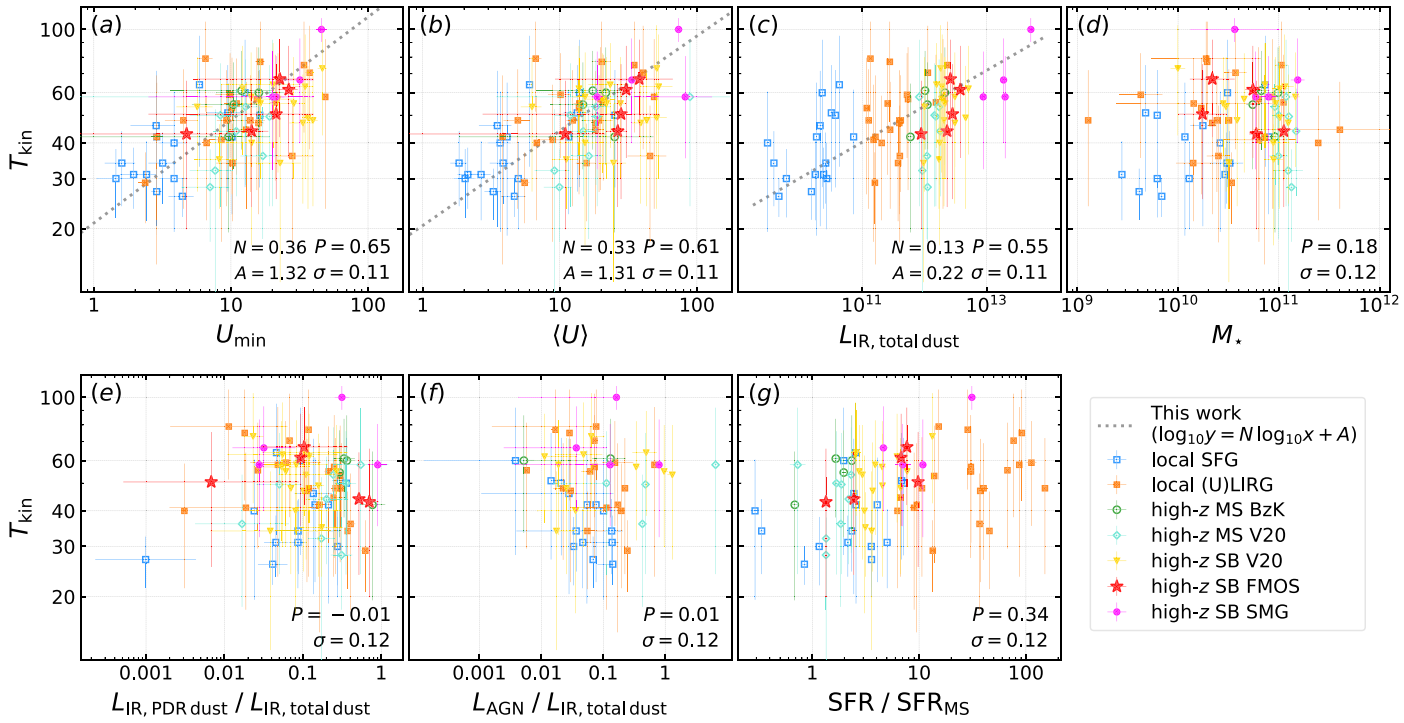

Figure 9. Fitted T_{kin} vs. galaxy properties, as in Figure 2. T_{kin} is shown as median and error bars representing the 1σ range of our model grid fitting to the observed R_{52} as presented in Section 5.

Yet this finding might also be limited by sample size and selection method, templates used for SED fitting, and the dust optically thin assumption in DL07 templates (e.g., Jin et al. 2019; Cortzen et al. 2020).

Combining with the results from this work, the T_{dust} or $\langle U \rangle$ trends are easier to understand when correlating them with molecular gas mean density and temperature. We propose a picture in which the general increase of dust temperature and ISRF is mainly due to the increase in cold molecular gas temperature, due to either higher CMB temperature at higher redshifts or more intense star formation and feedback. While the mean molecular gas density has a weaker, nonlinear trend driving $\langle U \rangle$ in most galaxies, merger-driven compaction could strongly increase gas density and hence boost $\langle n_{H_2} \rangle$, T_{kin}, and $\langle U \rangle$ in a small number of SB galaxies.

Such an increase in gas density creates more contrast at lower redshifts owing to the general decrease of the cosmic molecular gas density and CMB temperature. This could explain why $\langle U\rangle$ is more different between MS and SB galaxies at lower redshifts.

6.2. Density- or Temperature-regulated Star Formation? The $\langle U\rangle$–$\langle n_{\rm H_2}\rangle$ and $\langle U\rangle$–T_{kin} Correlations

Figures 8 and 9 show that both $\langle n_{\rm H_2}\rangle$ and $T_{\rm kin}$ positively correlate with U and $L_{\rm IR}$ but not with other properties like stellar mass or AGN fraction in our sample. Yet $\langle n_{\rm H_2}\rangle$ correlates with U or $L_{\rm IR}$ in a nonlinear way. Except for high-z SMGs and a few local galaxies with large error bars coming from their large R_{52} uncertainties, most galaxies are constrained within a narrow range of $\langle n_{\rm H_2}\rangle \sim 10^2$–$10^3$ cm^{-3}. Despite the large scatter in the data, we observe a trend with $n_{\rm H_2} \propto \langle U\rangle^{0.70}$ that seems to hold only within the intermediate $\langle U\rangle$ range ($\langle U\rangle \sim$ 5–20).

Meanwhile, $T_{\rm kin}$ has a tighter correlation ($\sigma \sim 0.11$) with U and $L_{\rm IR}$. We find relations $T_{\rm kin} \propto \langle U\rangle^{0.33}$ and $T_{\rm kin} \propto L_{\rm IR}^{0.13}$. Note that by calculating the [CI] $^3P_2$–$^3P_1$ and $^3P_1$–$^3P_0$ excitation temperatures as a probe of gas kinetic temperature under thermalized conditions, Jiao et al. (2017, 2019) and Valentino et al. (2020b) also found positive correlation between the gas kinetic temperature and dust temperature that is proportional to $\langle U\rangle^{0.16}$. There is also a weak trend that $T_{\rm kin}$ increases with SFR/SFR$_{\rm MS}$ (Pearson correlation coefficient $P = 0.34$), and the trend between $n_{\rm H_2}$ and SFR/SFR$_{\rm MS}$ is also marginal ($P = 0.40$).

Given these results, it is very reasonable that both mean gas density and temperature increase from less to more intensively SFGs. Yet based on the data sets in this work, it is difficult to statistically decouple $\langle n_{\rm H_2}\rangle$ and $T_{\rm kin}$ and hence to measure well the shapes of $\langle U\rangle$–$\langle n_{\rm H_2}\rangle$ and $\langle U\rangle$–$T_{\rm kin}$ correlations. However, the nonlinear or broken $\langle U\rangle$–$\langle n_{\rm H_2}\rangle$ correlation and the more smooth $\langle U\rangle$–$T_{\rm kin}$ might imply two scenarios, one for "normal" SFGs and one for merger-driven SBs. "Normal" galaxies may have a smooth density- and temperature-regulated star formation, whereas strong gas compression in major merger events can induce extraordinarily high $\langle n_{\rm H_2}\rangle$ with moderate $T_{\rm kin}$ and $\langle U\rangle$ (e.g., Tacconi et al. 2008; Engel et al. 2010; Riechers et al. 2010; Cooray et al. 2014; Larson et al. 2016; Calabrò et al. 2019). Further insights will require higher-quality, multiple-transition CO SLEDs, as we briefly discuss below (Section 6.4).

6.3. Implication for Star Formation Law Slopes

The star formation law is known as the correlation between gas mass (or surface density) and SFR (or surface density) and can be expressed as

$$\begin{aligned} {\rm SFR} &= A \cdot M_{\rm H_2}^N \quad \text{or} \\ \Sigma_{\rm SFR} &= A \cdot \Sigma_{\rm gas}^N, \end{aligned} \tag{5}$$

where A is the normalization and N is the slope. After the initial idea presented by Schmidt (1959), Kennicutt (1998) first systematically measured the star formation law to be $\Sigma_{\rm SFR} \propto \Sigma_{\rm gas}^{1.4\pm0.15}$ based on observations of nearby spiral and SB galaxies, where $\Sigma_{\rm gas}$ is the mass surface density of atomic plus molecular gas, and $\Sigma_{\rm SFR}$ is the SFR surface density traced by Hα and/or $L_{\rm IR}$. This Kennicutt–Schmidt law with $N \approx 1.4$ has been extensively studied in galaxies with $\Sigma_{\rm gas} \sim 1$–$10^5\,M_\odot\,{\rm pc}^{-2}$ and is widely used in numerical simulations (see reviews by Kennicutt & Evans 2012; Carilli & Walter 2013).

However, the actual slope N of the star formation law has been long debated. High-resolution (subkiloparsec-scale) observations in nearby spiral galaxies revealed that atomic gas does not correlate with SFR, whereas only molecular gas traces SFR, and N is close to unity in these galaxies (e.g., Wong & Blitz 2002; Bigiel et al. 2008; Leroy et al. 2008, 2013; Schruba et al. 2011). Meanwhile, from local SFGs to (U) LIRGs, observations suggest that N is superlinear, ranging from $\sim$1 to $\sim$2 (e.g., Kennicutt 1998; Yao et al. 2003; Gao & Solomon 2004a; Shetty et al. 2013, 2014b, 2014a; de los Reyes & Kennicutt 2019; Wilson et al. 2019). Furthermore, Daddi et al. (2010b) and Genzel et al. (2010) found that high-redshift MS and SB galaxies follow two parallel sequences in the star formation law ($M_{\rm H_2}$–SFR) diagram, each with substantial breadth, and both with $N \sim 1.1$–1.2 but with a 0.6 dex mean offset in normalization. Thus, why local SFG regions show a linear star formation law, while high-z SB galaxies have a much higher SFE $\equiv$ SFR/$M_{\rm H_2}$, is still to be understood.

Here we decompose the star formation law into $\langle U\rangle$ and $\langle n_{\rm H_2}\rangle$ to gain some insights. First, it is known that the dust-obscured SFR can be traced by the IR luminosity (e.g., Kennicutt 1998; Kennicutt & Evans 2012) as SFR $= L_{\rm IR}/C_{\rm IR}$, where $C_{\rm IR} \sim 10^{10}$ [$L_\odot$ ($M_\odot$yr^{-1})$^{-1}$] assuming a Chabrier (2003) IMF. Second, as mentioned in the previous section, $\langle U\rangle = P_0^{-1} \cdot L_{\rm IR}/M_{\rm dust}$. Third, we use the gas-to-dust ratio $\delta_{\rm GDR} \equiv M_{\rm gas}/M_{\rm dust}$ to link gas to dust mass. This ratio varies with metallicity (e.g., Israel 1997; Leroy et al. 2007, 2011; Bolatto et al. 2013; Sandstrom et al. 2013; Rémy-Ruyer et al. 2014, 2015), and also note that the definition of gas in $\delta_{\rm GDR}$ is atomic plus molecular gas. We include an additional molecular hydrogen fraction $f_{\rm H_2} \equiv M_{\rm H_2}/M_{\rm gas}$ to the gas-to-dust ratio, having finally $M_{\rm dust} = M_{\rm H_2} \cdot (f_{\rm H_2}\,\delta_{\rm GDR})^{-1}$. Fourth, we consider MS galaxies to be disks with radius r and height h and assume that $\langle n_{\rm H_2}\rangle$ is the global mean gas density; thus, the molecular gas mass can be expressed as the product of the volume and the mean molecular gas density: $M_{\rm H_2} = \pi \cdot \langle n_{\rm H_2}\rangle \cdot r^2 \cdot h$. And fifth, we ignore atomic gas and only consider the molecular gas star formation law.

Then, we rewrite the star formation law equation as

$$\begin{aligned} {\rm SFR} &= A \cdot M_{\rm H_2}^N \\ &\Rightarrow \langle U\rangle \cdot M_{\rm dust} = A \cdot P_0^{-1} \cdot C_{\rm IR} \cdot M_{\rm H_2}^N \\ &\Rightarrow \langle U\rangle \cdot (f_{\rm H_2}\,\delta_{\rm GDR})^{-1} = A \cdot P_0^{-1} \cdot C_{\rm IR} \cdot M_{\rm H_2}^{N-1} \\ &\Rightarrow \langle U\rangle \cdot (f_{\rm H_2}\,\delta_{\rm GDR})^{-1} \\ &= A \cdot P_0^{-1} \cdot C_{\rm IR} \cdot (\pi \cdot \langle n_{\rm H_2}\rangle \cdot r^2 \cdot h)^{N-1}. \end{aligned} \tag{6}$$

Taking the logarithm of both sides, and assuming that $\log\langle U\rangle$, $\log(f_{\rm H_2}\,\delta_{\rm GDR})$, and $\log(r^2\,h)$ are functions of $\log\langle n_{\rm H_2}\rangle$, we have

$$\begin{aligned} &\log\langle U\rangle - \log(f_{\rm H_2}\,\delta_{\rm GDR}) \\ &= \log(A\,P_0^{-1}\,C_{\rm IR}) + (N-1)[\log\langle n_{\rm H_2}\rangle + \log(\pi r^2 h)] \\ &\Rightarrow N = \frac{\frac{d\log\langle U\rangle}{d\log\langle n_{\rm H_2}\rangle} - \frac{d\log(f_{\rm H_2}\,\delta_{\rm GDR})}{d\log\langle n_{\rm H_2}\rangle}}{1 + \frac{d\log(r^2 h)}{d\log\langle n_{\rm H_2}\rangle}} + 1. \end{aligned} \tag{7}$$

Therefore, the star formation law slope N depends on how $\langle U\rangle$, $f_{\rm H_2}\,\delta_{\rm GDR}$ (metallicity), and $r^2 h$ (galaxy size) change with $\langle n_{\rm H_2}\rangle$, which can further be described by the differentials $\frac{d\log\langle U\rangle}{d\log\langle n_{\rm H_2}\rangle}$, $\frac{d\log(f_{\rm H_2}\,\delta_{\rm GDR})}{d\log\langle n_{\rm H_2}\rangle}$, and $\frac{d\log(r^2 h)}{d\log\langle n_{\rm H_2}\rangle}$, respectively. These differentials

strongly depend on galaxy samples. When studying subkiloparsec regions in local SFGs, if the ISRF, metallicity, and galaxy size are similar among these SFGs, N is close to 1. When studying a sample including both SFGs and (U)LIRGs, $\langle U\rangle$ increases by a factor of a few tens with $\langle n_{\rm H_2}\rangle$ changing from 10^2 to $10^4\,{\rm cm}^{-3}$, and r decreases by a factor of a few with $\langle n_{\rm H_2}\rangle$, as (U)LIRGs are usually smaller and more compact (while the scale height h seems constant; e.g., Wilson et al. 2019). As for the $f_{\rm H_2}\,\delta_{\rm GDR}$ term, because $f_{\rm H_2}$ increases with metallicity while $\delta_{\rm GDR}$ decreases with it, their product $f_{\rm H_2}\,\delta_{\rm GDR}$ likely does not change much. Therefore, N can be much higher than 1. The overall effect is that the star formation law does not have a single slope, yet the overall N is about 1–2.

6.4. Limitations and Outlook

We discuss three limitations of this work: the overall quality of current data sets, the assumptions in the gas modeling, and the contamination from AGNs. First, CO line ratio or SLED studies require two or more CO line observations. These observations have different observing conditions, beam sizes, flux calibrations, etc.; thus, uncertainties are very likely underestimated even when the S/Ns of the line measurements are formally large (e.g., >3). For example, for our local SFG subsample, CO (5–4) data are from the Herschel FTS with a certain beam size of ∼40″, which does not match the mapping area of CO (2–1) from ground-based telescopes. The correction from the FTS beam to the entire galaxy can have a factor of two difference, which is reflected in the scatter of our data points although not fully reflected in their error bars. The absolute flux calibration uncertainty of the observations in the literature can also be as high as ∼30%, which is much poorer than current IRAM 30 m and ALMA (total power) observations (<10%). This also increases the scatter in our plots and necessarily makes observed correlations less significant. As for high-redshift galaxies, we use an S/N of 3 in both CO lines to select our sample, which usually only reflects the quality of line measurements, while it does not include the absolute flux calibration uncertainty. Their dust SEDs are also much more poorly covered; thus, their $\langle U\rangle$ have fairly large uncertainties. Future ALMA Band 3–8 mapping of CO lines from $J_{\rm u}=1$ to 4 in local galaxies and VLA plus ALMA observations for suitable galaxies at high redshift with high-quality CO and continuum data will be the key to both spatially understand and statistically verify correlations between $\langle U\rangle$, $\langle n_{\rm H_2}\rangle$, and $T_{\rm kin}$, as well as to unveil any evolutionary trend with redshift.

Second, our assumptions in the gas modeling are also simplistic, in order to reflect only the effects of density and temperature on CO excitation. The constant $\alpha_{\rm vir}$ assumption does not reflect the real situation in galaxies, e.g., as shown in Sun et al. (2018). Doubling the $\alpha_{\rm vir}$ value from what we use in this work will result in a 20% lower R_{52} at $\log_{10}(\langle n_{\rm H_2}\rangle/{\rm cm}^{-3})=3$, $T_{\rm kin}=25$ K, and $z=0$. The constant $T_{\rm kin}$ assumption for all one-zone clouds in a galaxy is also a simplified "toy model"-like condition. Adopting more realistic assumptions from observations (e.g., Sun et al. 2020) or from hydrodynamic+chemistry simulations (e.g., Smith et al. 2014a, 2014b, 2016, 2020; Tress et al. 2020) in our gas modeling would naturally be the next step.

Third, it is known that some galaxies host AGNs that significantly contribute to optical or mid-IR SEDs, as well as affect the CO excitation. Our SED fitting has already included a mid-IR AGN component that can dominate rest-frame 5–50 μm emission. This substantially improves the fitting χ^2 for a number of galaxies showing mid-IR power-law SED features, which, however, also brings in larger uncertainties in $\langle U\rangle$ as reflected in the error bars in our plots. The used AGN SED templates could also slightly affect our results, although this effect should be well captured by the quoted uncertainties. Additional mid-IR photometry from future space telescopes like the James Webb Space Telescope (JWST) and the Origins Space Telescope (OST) will be key to solve this degeneracy and provide accurate AGN/ISRF decomposition. Meanwhile, an AGN can also boost highly excited CO lines within X-ray-dominated regions (XDRs) as shown by $J_{\rm u}\gtrsim 9$ CO studies (e.g., van der Werf et al. 2010; Rangwala et al. 2011; Hailey-Dunsheath et al. 2012; Spinoglio et al. 2012; Meijerink et al. 2013; Pereira-Santaella et al. 2013; Rosenberg et al. 2014a). Decomposition of such AGN-dominated CO SLEDs usually requires three components, but the XDR component starts to dominate the CO SLED only at $J_{\rm u}\gtrsim 9$. Thus, for this work, at CO (5–4) AGNs likely contribute less than 10% (e.g., see Figure 2 of van der Werf et al. 2010).

7. Summary

In this work, we compiled a comprehensive sample of galaxies from local to high redshift with CO (2–1) and CO (5–4) detections and well-sampled IR SEDs. This includes our new IRAM PdBI CO (5–4) observations of six $z\sim 1.5$ COSMOS SB galaxies. With this large sample, we measure their mean ISRF intensity $\langle U\rangle$ from dust SED fitting (Section 3) and their mean molecular gas density $\langle n_{\rm H_2}\rangle$ converted from $R_{52}=S_{\rm CO(5\text{-}4)}/S_{\rm CO(2\text{-}1)}$ line ratios based on our density–PDF gas modeling (Section 5). Our results can be summarized as follows.

1. We confirm the tight $\langle U\rangle$–R_{52} correlation first reported by Daddi et al. (2015) and find that $\langle U\rangle$, $U_{\rm min}$, and $L_{\rm IR}$ all strongly correlate with R_{52}, while stellar mass, AGN fraction, and the SFR offset to the MS all show weaker or no correlation with R_{52} (Figure 2).
2. We conduct density–PDF gas modeling to connect the mean molecular gas density $\langle n_{\rm H_2}\rangle$ and kinetic temperature $T_{\rm kin}$ to the observable CO line ratio R_{52}. Based on this, we provide a Monte Carlo method (and a PYTHON package `co-excitation-gas-modeling`) to compute $\langle n_{\rm H_2}\rangle$ and $T_{\rm kin}$'s probability ranges using our model grid for any given $J_{\rm u}=1$–10 CO line ratio (and for CO SLED as the next step; see, e.g., Figure 6).
3. We find that both $\langle n_{\rm H_2}\rangle$ and $T_{\rm kin}$ increase with $\langle U\rangle$, with $T_{\rm kin}$ having a tighter correlation with $\langle U\rangle$.
4. Based on these correlations, we propose a scenario in which the ISRF in the majority of galaxies is more directly regulated by the gas temperature and nonlinearly by the gas density. A fraction of SB galaxies have gas densities larger by more than one order of magnitude with respect to MS galaxies and are possibly in a merger-driven compaction stage (Sections 6.2 and 6.1).
5. We link the $\langle U\rangle$–$\langle n_{\rm H_2}\rangle$ correlation to the Kennicutt–Schmidt star formation law and discuss how the star formation law slope N can be inferred from the $\langle U\rangle$–$\langle n_{\rm H_2}\rangle$ correlation slope and other galaxy properties versus $\langle n_{\rm H_2}\rangle$ correlations. We find that $N\sim$ 1–2 can be inferred from

the trends of how $\langle U \rangle$ and galaxy size change with $\langle n_{H_2} \rangle$ in different galaxy samples (Section 6.3).

Our study demonstrates that ISRF and molecular gas are tightly linked to each other, and density–PDF gas modeling is a promising tool for probing detailed ISM physical quantities, i.e., molecular gas density and temperature, from observables like CO line ratios/SLEDs.

We thank the anonymous referee for helpful comments. D. L., E.S., and T.S. acknowledge funding from the European Research Council (ERC) under the European Union's Horizon 2020 research and innovation program (grant agreement No. 694343). F.V. acknowledges support from the Carlsberg Foundation Research Grant CF18-0388 "Galaxies: Rise and Death". G.E.M. and F.V. acknowledge the Villum Fonden research grant 13160 "Gas to stars, stars to dust: tracing star formation across cosmic time" and the Cosmic Dawn Center of Excellence funded by the Danish National Research Foundation under then grant No. 140. Y.G.'s research is supported by the National Key Basic Research and Development Program of China (grant No. 2017YFA0402700), National Natural Science Foundation of China (grant Nos. 11861131007, 11420101002), and Chinese Academy of Sciences Key Research Program of Frontier Sciences (grant No. QYZDJSSW-SLH008). S.J. acknowledges financial support from the Spanish Ministry of Science, Innovation and Universities (MICIU) under grant AYA2017-84061-P, co-financed by FEDER (European Regional Development Funds). A.P. gratefully acknowledges financial support from STFC through grants ST/T000244/1 and ST/P000541/1. We thank A. Weiss and C. Wilson for helpful discussions. This work used observations carried out under project No. W14DS with the IRAM Plateau de Bure Interferometer (PdBI). IRAM is supported by INSU/CNRS (France), MPG (Germany), and IGN (Spain). This work used observations carried out under project 17A-233 with the National Radio Astronomy Observatory's Karl G. Jansky Very Large Array (VLA). The National Radio Astronomy Observatory is a facility of the National Science Foundation operated under cooperative agreement by Associated Universities, Inc.

Data Availability

Our MICHI2 SED fitting code is publicly available at https://ascl.net/code/v/2533. Our PYTHON package `co-excitation-gas-modeling` for computing $\langle n_{H_2} \rangle$ and T_{kin} from CO line ratios is publicly available at https://pypi.org/project/co-excitation-gas-modeling. And our SED fitting figures as shown in Figure 1 and the full Table 1 are publicly available at 10.5281/zenodo.3958271.

Appendix A
IRAM PdBI CO Observations of $z \sim 1.5$ FMOS-COSMOS Galaxies

We present the sample table and CO (5–4) imaging of our PdBI observations in Table 2 and Figure 10. The observations are described in Section 2.2.

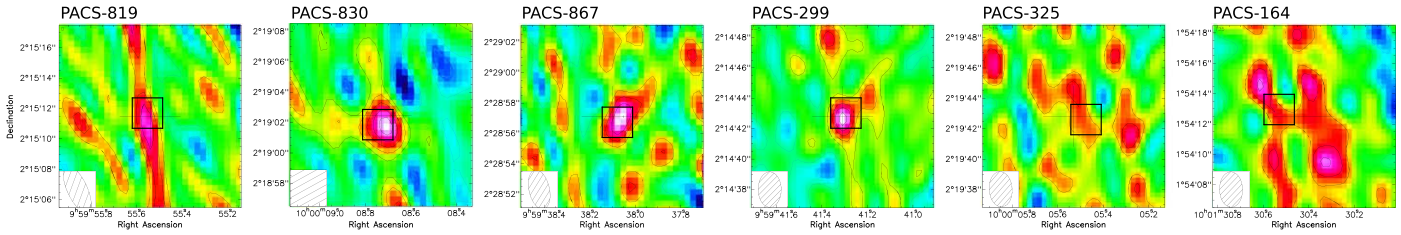

Figure 10. CO (5–4) line maps for PACS-819, PACS-830, PACS-867, PACS-299, PACS-325, and PACS-164, respectively. In the last two panels, PACS-325 and PACS-164 are undetected. The field of view is $12'' \times 12''$ in all panels. Contours have a spacing of 1σ noise in each panel. The cross-hair indicates the phase center, and the box indicates the ALMA CO (2–1) emission peak position, which is also the position where we extract the CO (5–4) line fluxes.

Table 2
CO Observation Results

Source	R.A.$_{CO}$	Decl.$_{CO}$	z_{CO}	ΔV_{CO} (km s^{-1})	CO Size ($''$)	$S_{CO(1-0)}$ (Jy km s^{-1})	$S_{CO(2-1)}$ (Jy km s^{-1})	$S_{CO(5-4)}$ (Jy km s^{-1})
(1)	(2)	(3)	(4)	(5)	(6)	(7)	(8)	(9)
PACS-819	09:59:55.552	02:15:11.70	1.4451	592	0.335	⋯	1.10 ± 0.07	3.850 ± 0.922
PACS-830	10:00:08.746	02:19:01.87	1.4631	436	0.973	⋯	1.18 ± 0.10	1.876 ± 0.387
PACS-867	09:59:38.078	02:28:56.73	1.5656	472	⋯	0.119 ± 0.064	0.46 ± 0.04	0.731 ± 0.218
PACS-299	09:59:41.295	02:14:43.03	1.6483	590	⋯	<0.210[a]	0.67 ± 0.08	1.758 ± 0.325
PACS-325	10:00:05.475	02:19:42.61	1.6538	764	⋯	⋯	0.28 ± 0.06	<0.942[a]
PACS-164	10:01:30.530	01:54:12.96	1.6481	894	⋯	<0.222[a]	0.61 ± 0.11	1.175 ± 0.465

Notes. Columns (1–6) and (8) are the ALMA CO (2–1) properties reported by Silverman et al. (2015b). Columns (7) and (9) show the results from this work for VLA CO (1–0) and IRAM PdBI CO (5–4), respectively.
[a] 3σ upper limits.

Appendix B
Some Notes on CO Observations of Individual Nearby Galaxies in the Literature

CenA. We excluded this galaxy because its CO (2–1) and CO (5–4) data only cover the center of the galaxy, and significant correction is needed for recovering the entire galaxy. For example, Kamenetzky et al. (2014) applied a correction factor of $1/0.48$, where 0.48 is the beam-aperture-to-entire-galaxy fraction denoted as "BeamFrac" and reported in the full Table 1 (available online), to convert the CO (2–1) observed at the galaxy center with a beam of 22″ (Eckart et al. 1990) to a beam of 43″ for their study. They derived this factor based on SPIRE 250 μm image aperture photometry. Based on PACS 70–160 μm (as presented in L15), we obtain correction factors of $1/0.088$ and $1/0.185$ from a 22″ and 43″ beam to the entire galaxy, respectively. Thus, the 22″-to-43″ correction factors in two works fully agree ($0.088/0.185 \approx 0.48$). Despite the good agreement in beam-related correction among these works, we caution that using far-infrared data to correct CO (2–1) is very uncertain, as low-J CO lines do not linearly correlate with far-infrared emission (L15).

M83. We excluded this galaxy in this work as well. Israel & Baas (2001) reported a CO (2–1) line flux of 261 ± 15 K km s^{-1} (5501 ± 316 Jy km s^{-1}) within a 22″ beam (with SEST 15 m) at the M83 galaxy center, Lundgren et al. (2004) reported 98.1 ± 0.8 K km s^{-1} (2068 ± 17 Jy km s^{-1}) within a 22″ aperture (with JCMT 15 m) at the same center, and Bayet et al. (2006) reported 67.4 ± 2.2 K km s^{-1} (2721 ± 88 Jy km s^{-1}) within a 30.″5 beam (with CSO 10.4 m) also at the center position. Kamenetzky et al. (2014) adopted the Bayet et al. (2006) line flux and applied a factor of $1/0.76$ correction to obtain the line flux within a 43″ beam. This correction factor agrees with L15. However, if we want to obtain the entire flux for M83, we will need to correct the 43″ flux by a factor of $1/0.232$ based on the Herschel PACS aperture photometry in L15. We caution that the uncertainty in such a correction is large, and the CO (2–1) line fluxes at the galaxy center in the literature are already inconsistent by a factor of two.

NGC 0253. At the galaxy center position, the reported CO (2–1) line fluxes are 6637 ± 996 Jy km s^{-1} within a 12″ beam (Bradford et al. 2003), $10{,}684 \pm 1602$ Jy km s^{-1} within a 15″ beam (Bradford et al. 2003), $17{,}757 \pm 3551$ Jy km s^{-1} within a 21″ beam (Bayet et al. 2004), $24{,}428 \pm 2686$ Jy km s^{-1} within a 23″ beam (Bayet et al. 2004), $33{,}800 \pm 3200$ Jy km s^{-1} within a 43.″5 beam (Kamenetzky et al. 2014), and $34{,}300 \pm 3600$ Jy km s^{-1} within a 43.″5 beam (Kamenetzky et al. 2014; corrected from the original beam in Harrison et al. 1999). The beam-to-entire-galaxy fraction, "BeamFrac," is 0.518 from 43.″5 to the entire galaxy based on L15. These fluxes are roughly consistent, and the "BeamFrac"-based correction factor is only a factor of two; thus, we take the last 43.″5 beam flux and obtain $66{,}216 \pm 15010$ Jy km s^{-1} as the CO (2–1) flux for the entire NGC 0253, where we added a 0.2 dex uncertainty to the 43.″5 beam flux error. We caution that, even with the additional uncertainty, the flux error might still underestimate the true uncertainty, which includes original flux calibration and measurement error in Harrison et al. (1999), correction from original beam to 43.″5 by Kamenetzky et al. (2014), and correction from 43.″5 beam to entire galaxy by L15.

NGC 0891. We excluded this galaxy in this work. Braine & Combes (1992) reported a CO (2–1) line flux of 86 ± 6 K km s^{-1} (1974 ± 138 Jy km s^{-1}) within a convolved 23″ beam at the galaxy center position. Baan et al. (2008) converted the same line brightness temperature from Braine & Combes (1992) to a flux of 381 ± 26 Jy km s^{-1}, which, however, is lower than our converted value in parentheses and is possibly mistaking the original 12″ beam for calculation, while the brightness temperature that Braine & Combes (1992) reported has been convolved to 23″ beam as mentioned in their Table 1 caption. We note that the correction factor from 12″ or 23″ to the entire NGC 0891 is as large as ∼10, e.g., the "BeamFrac" from 16.″9 to entire galaxy is 0.112 as measured by L15. Thus, it is too uncertain to consider this galaxy in this work.

As for CO (1–0), Braine & Combes (1992) reported a line flux of 96 ± 5 K km s^{-1} (551 ± 28 Jy km s^{-1}) within a 23″ beam at the galaxy center position. This can be corrected to the entire galaxy scale as 3908 ± 204 Jy km s^{-1} based on L15. Gao & Solomon (2004a, 2004b) reported a line flux of 35.5 ± 5 K km s^{-1} (963 ± 136 Jy km s^{-1}) within a 50″ beam (with FCRAO 14 m) and a global scale integrated flux of 3733.7 Jy km s^{-1}. They are consistent within errors.

NGC 1068. Braine & Combes (1992) reported a CO (2–1) line flux of 240 ± 10 K km s^{-1} (5488 ± 229 Jy km s^{-1}) within a convolved 23″ beam at the galaxy center position. Baan et al. (2008) converted the same line brightness temperature from Braine & Combes (1992) to a flux of 1967.2 ± 80 Jy km s^{-1}, which is also inconsistent with our converted value (in parentheses) and possibly due to the mistaking of the original 12″ beam in their calculation. Papadopoulos et al. (2012) reported a CO (2–1) line flux of 11300 ± 2200 Jy km s^{-1} within the inner 40″ of NGC 1068 (originally from Papadopoulos & Seaquist 1999). Kamenetzky et al. (2011) reported a CO (2–1) line flux of 8366 ± 19 Jy km s^{-1} within a beam of 30″ (with CSO 10.4 m), which is then corrected to 43″-beam flux of $11{,}700 \pm 1100$ Jy km s^{-1} by Kamenetzky et al. (2014). Kamenetzky et al. (2014) also cited the Baan et al. (2008) flux and reported a 43″-beam flux of $12{,}600 \pm 2500$ Jy km s^{-1} converted from a 12″ beam. But note that Baan et al. (2008) might have mistaken a 12″ beam for the calculation. If we directly correct the Braine & Combes (1992) 23″-beam flux to a 43″ beam, it is 8669 Jy km s^{-1}, which, however, is 30% smaller than that in Kamenetzky et al. (2014). Meanwhile, if we correct the Kamenetzky et al. (2011) flux from 30″ beam to 43″ beam, it is 10,542 Jy km s^{-1}, consistent with both Kamenetzky et al. (2014) and Papadopoulos et al. (2012). Given that the difference is only about 30%, in this work we adopt the average of these fluxes, i.e., 10170 Jy km s^{-1} for a 43″ beam, or 15,551 Jy km s^{-1} corrected to the entire galaxy scale (based on L15 BeamFrac).

For CO (1–0), we perform our own photometry using the Nobeyama 45 m COAtlas Survey data (Kuno et al. 2007) and obtain a flux of 5228 Jy km s^{-1}. This is 40% higher than the global scale line flux of 3651.1 Jy km s^{-1} measured by Gao & Solomon (2004b) using FCRAO mapping observations, but closer to the line flux of 4240 Jy km s^{-1} within a 43″ beam reported by Kamenetzky et al. (2014), which is citing Baan et al. (2008) and originally also from Gao & Solomon (2004b).

NGC 1365. NGC 1365 were observed at two positions by Herschel SPIRE FTS, one at northeast (NGC 1365-NE) and one at southwest (NGC 1365-SW). They have similar CO (5–4) within 10%, but the IR luminosities within each aperture differ by 25%. This means that our aperture-based beam-to-entire-galaxy correction has at least 25% uncertainty (same in the independent analysis of the similar method by Kamenetzky et al. 2014). For CO (2–1) we use the same Sandqvist et al. (1995) SEST 15 m (24″ beam) data as in Kamenetzky et al. (2014) and

correct it to the entire galaxy scale to match our corrected CO (5–4).

NGC 1614. CO (2–1) is from Aalto et al. (1995), observed with SEST 15 m (22″ beam; $\eta_{\rm mb}=0.5$, $\int T_{\rm mb}dv=56\pm2$ K km s^{-1} or line flux 1180 ± 42 Jy km s^{-1}). We correct from 22″ beam to the entire galaxy with a BeamFrac of 0.792 (L15). Meanwhile, note that Wilson et al. (2008) reported an interferometric integrated CO (2–1) flux of 670 ± 7 Jy km s^{-1} (synthesized beam $3\farcs7\times3\farcs3$). The discrepancy of about 50% is likely due to the missing flux of the interferometry (see Wilson et al. 2008).

NGC 2369. CO (2–1) is from Aalto et al. (1995), observed with SEST 15 m (22″ beam; $\eta_{\rm mb}=0.5$, $\int T_{\rm mb}dv=74\pm2.4$ K km s^{-1}, or line flux 1560 ± 51 Jy km s^{-1}). Meanwhile, note that Baan et al. (2008) reported 959.4 ± 14.3 Jy km s^{-1}, which is originally from Garay et al. (1993) also with SEST 15 m ($\int T_{\rm mb}dv=46.8\pm0.7$ K km s^{-1}, with $\eta_{\rm mb}=0.54$). The reason for this factor of two discrepancy is unclear. Here we take their average (1259.7 Jy km s^{-1}) and correct from the 22″ beam to the entire galaxy with a BeamFrac of 0.808 (L15).

NGC 2623. Wilson et al. (2008) reported an interferometric integrated CO (2–1) flux of 267 ± 8 Jy km s^{-1} observed with SMA. Papadopoulos et al. (2012) cited this flux in their study and discussed that this flux is unlikely affected by missing flux.

NGC 3256. Aalto et al. (1995) reported a CO (2–1) flux of $\int T_{\rm mb}dv=314\pm8$ K km s^{-1} (6619 ± 169 Jy km s^{-1}) observed with SEST 15 m (22″ beam; $\eta_{\rm mb}=0.5$). Meanwhile, Baan et al. (2008) reported 2980.7 ± 14.3 Jy km s^{-1}, which is originally from Garay et al. (1993), also observed with SEST 15 m ($\int T_{\rm mb}dv=145.5\pm0.7$ K km s^{-1}, with $\eta_{\rm mb}=0.7$). Similar to NGC 2369, the reason for the factor of two to three discrepancy is unclear. We take their average (4799.85 Jy km s^{-1}) and correct from the 22″ beam to the entire galaxy with a BeamFrac of 0.744 (L15).

NGC 3351. We obtain CO (2–1) and CO (1–0) line fluxes for the entire galaxy with our own photometry as 2681 and 1138 Jy km s^{-1}, respectively, to the HERACLES data and the Nobeyama 45 m COAtlas Survey (Kuno et al. 2007) data. Uncertainties contributed by the noise in the moment-0 maps are about 6% of the measured fluxes. Note that Braine & Combes (1992) observed a CO (2–1) and CO (1–0) flux of about 642 and 97 Jy km s^{-1}, respectively, convolved to a 23″ beam. Leroy et al. (2009) reported a CO (2–1) luminosity of 0.78×10^5 K km s^{-1} arcsec^2, or a line flux of 2808 Jy km s^{-1}, for the entire galaxy, consistent with ours. Usero et al. (2015) reported a CO (1–0) flux of about 210 Jy km s^{-1} within a $21\farcs3$ beam at the central position.

NGC 3627. Similar to NGC 3351, we obtain the CO (2–1) and CO (1–0) line fluxes for the whole galaxy via our photometry using the HERACLES and the NRO45 m COAtlas data, respectively. We measured 9219 and 7366 Jy km s^{-1}, respectively. Note that Gao & Solomon (2004b) reported a global CO (1–0) flux of 4477 Jy km s^{-1}, which is about 40% lower than ours.

NGC 4321. Similar to NGC 3351 and NGC 3627, the global CO (2–1) and CO (1–0) line fluxes are obtained as 9088 and 2251 Jy km s^{-1}, from the HERACLES and the NRO45 m COAtlas data, respectively. Note that Braine & Combes (1992) observed a CO (1–0) flux of 445 Jy km s^{-1} within a 23″ beam, which can be corrected to a consistent entire galaxy flux of 2280 Jy km s^{-1} by a BeamFrac of 0.195 (L15), while Komugi et al. (2008) observed a CO (1–0) flux of 174 Jy km s^{-1} within a 16″ beam, which is somehow lower than others.

NGC 4945. Wang et al. (2004) observed the central position of NGC 4945 with SEST 15 m and obtained a CO (2–1) flux of $\int T_{\rm mb}dv=920.9\pm0.6$ K km s^{-1} ($19{,}412\pm12.6$ Jy km s^{-1}, for point-source response in a 22″ beam). Baan et al. (2008) cited the same Wang et al. (2004) CO (2–1) flux as $18{,}878.5\pm12.3$ Jy km s^{-1}, which is consistent with our conversion. Curran et al. (2001) also observed the central position of NGC 4945 with SEST 15 m. They reported a CO (2–1) flux of $\int T_{\rm mb}dv=740\pm40$ K km s^{-1}, about 20% lower than that of Wang et al. (2004). As discussed in Wang et al. (2004), the reason for the discrepancy is unclear, but this shows that the uncertainty in the CO (2–1) flux at the galaxy center is at least 20%. We take the average (17,505 Jy km s^{-1}) in this work and estimate the entire galaxy CO (2–1) flux to be 31,770 Jy km s^{-1} based on a BeamFrac of 0.551 (L15) from the 22″ beam.

NGC 6946. The global CO (2–1) and CO (1–0) line fluxes are obtained as 36,296 and 11,454 Jy km s^{-1}, from the HERACLES and the NRO45 m COAtlas data, respectively. This is in good agreement with the global scale CO (1–0) flux of 11,400.5 Jy km s^{-1} reported by Gao & Solomon (2004b) using NRAO 12 m mapping data.

Appendix C
Comparison of SED Fitting Codes

We performed additional MAGPHYS (da Cunha et al. 2008, 2015; Battisti et al. 2019) and CIGALE (Burgarella et al. 2005; Noll et al. 2009; Ciesla et al. 2014, 2015; Boquien et al. 2019; Yang et al. 2020) SED fitting to verify our MICHI2 SED fitting results. We use the updated MAGPHYS version with high-z extension (http://www.iap.fr/magphys/download.html), and CIGALE version 2020.0 (2020 June 29) (https://cigale.lam.fr/download/). We modified the MAGPHYS FORTRAN source code to allow for longer photometry filter names and larger filter number. MAGPHYS and CIGALE require a list of preset filters, for which we choose the following list: GALEX FUV and NUV, KPNO MOSAIC1 *u*, CFHT MegaCam *u* band, SDSS *ugriz*, Subaru SuprimeCam *BVriz*, GTC *griz*, VISTA VIRCAM *Y*, *J*, *H*, K_s, *HST* ACS F435W/F606W/F755W/F814W and WFC3 F125W/F140W/F160W, Spitzer IRAC ch1/2/3/4, IRS PUI 16 μm and MIPS 24 μm, Herschel PACS 70/100/160 and SPIRE 250/350/500 μm, SCUBA2 450/850 μm, VLA 3/1.4 GHz, and pseudo-880/1100/1200/2000 μm filters. Other photometry data like submillimeter interferometry data (e.g., from ALMA) and some optical data are ignored. Note that in our MICHI2 fitting these bands without a known filter curve are automatically used with a pseudo-delta-function filter curve.

The current MAGPHYS code does not include the fitting of a mid-IR AGN SED component, although such an extension has been used nonpublicly in some studies (Chang et al. 2015). MAGPHYS has preset stellar libraries, dust attenuation laws, and dust libraries; therefore, there is no need to adjust any parameters, except that we run MAGPHYS only for $z>0.03$ galaxies, as MAGPHYS computes the luminosity and mass properties with the luminosity distance, which does not match the physical distance at a very low z.

CIGALE has the capability of including a mid-IR AGN component, as does our MICHI2 code. The current version of CIGALE uses AGN emission models computed from physical modeling of AGN torus by Fritz et al. (2006). It has much more freedom than the observationally derived AGN templates by Mullaney et al. (2011) used by MICHI2. However, this can also easily overfit the data when there are only a few broadband

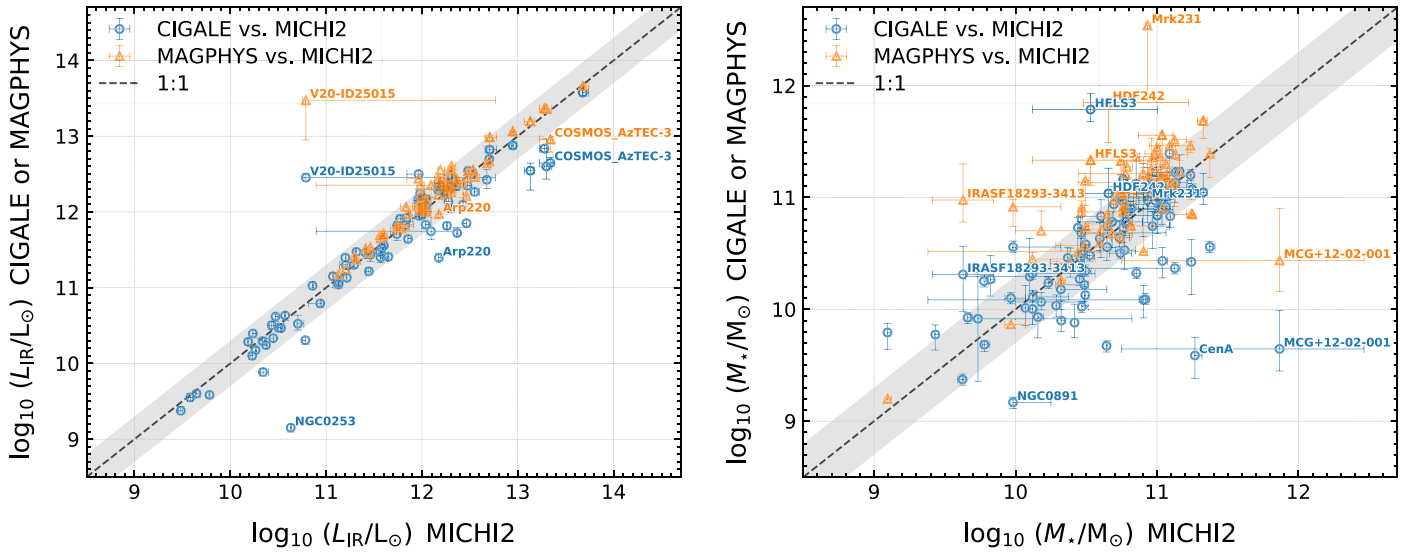

Figure 11. Comparison of the fitted 8–1000 μm dust luminosities (left panel) and stellar masses (right panel) from three SED fitting codes: MICHI2, CIGALE, and MAGPHYS. *X*-axes in both panels indicate the fitted parameters from the MICHI2, whereas *Y*-axes indicate those from either CIGALE (blue circles) or MAGPHYS (orange triangles). The dashed line is a one-to-one relation, and the gray shading indicates a $\pm$0.3 dex range. Error bars show the fitted 16th and 84th percentiles, and symbols center at the minimum-χ^2/highest-probability values.

photometry data points at mid-IR ~8–100 μm. For our fitting with CIGALE, we fix several AGN parameters based on the fitting results of SB galaxies in Fritz et al. (2006), `r_ratio = 60`, `beta = −1.0`, `gamma = 6.0`, `opening_angle = 140.0`, and let the following parameters vary: `tau = 1.0, 3.0, 6.0`, `psy = 0.001, 10.100, 20.100, 30.100`, and `fracAGN = 0.0, 0.2, 0.4, 0.6`.

For the stellar component in our CIGALE fitting of high-redshift galaxies, we use a constant SFH as in our MICHI2 fitting. This is achieved by adding `sfhperiodic` into the CIGALE `sed_modules` and setting `type_bursts = 2`, `delta_bursts = 200`, `tau_bursts = 200`. To allow the fitting of a range of stellar ages, we set `age = 200, 300, 400, 500, 600, 700, 800, 900, 1000, 2000` for the `bc03` SED module. And we adopt the Calzetti et al. (2000) dust attenuation law as in our MICHI2 fitting by adding `dustatt_modified_starburst` to the SED modules and setting `E_BV_lines` to 0.0 to 2.0 in steps of 0.2. Meanwhile, for local galaxies ($z < 0.03$) in our sample whose stellar ages are generally older, a constant SFH stellar component cannot fit the stellar SED well. Thus, we adopt the exponentially declining SFH `sfh2exp` in CIGALE and set `tau_main = 200, 500, 1000, 2000, 4000` and `age = 200, 500, 1000, 2000, 4000, 6000, 8000, 10000`. We turn off the burst model by setting `f_burst = 0.0`.

The dust template used in CIGALE fitting is also the same as used in our MICHI2 fitting, i.e., the Draine et al. (2014) updated DL07 templates. $U_{\rm min}$ (`umin`) is set to vary from 1.0 to 50, and $f_{\rm PDR}$ (`gamma`) from 0.0 to 1.0. We also set `lim_flag = True` to allow CIGALE to analyze the photometry upper limits (to achieve this, we need to flip the sign of the flux errors for the photometry with an S/N < 3). Then, each galaxy has about 696,960 models fitted. In comparison, in MAGPHYS in general 13,933 optical models and 24,999 IR dust models are fitted for each galaxy.

In Figure 11, we compare the fitted dust 8–1000 μm luminosities and stellar masses from the three SED fitting codes. In the left panel of Figure 12 we compare the fitted $\langle U \rangle$ from MICHI2 and CIGALE, as MAGPHYS does not have the same Draine & Li (2007) library. Note that not all fittings show a reasonable χ^2, as can be seen in the right panel of Figure 12, where the histograms of reduced-χ^2 are shown for the three fitting codes. CIGALE fittings in general have a higher reduced-χ^2, which means poorer fitting than MICHI2, whereas MAGPHYS produces slightly better fittings than MICHI2. However, both MAGPHYS and CIGALE have a number of very poor/failed fitting cases that have reduced-$\chi^2 \gtrsim 10$ and are the outlier data points in Figures 11. The threshold reduced-$\chi^2 \sim 8$–10 is empirically estimated after visually examining the SED fitting results.[29] There are only two sources that exhibit reduced-$\chi^2 > 10$ in MICHI2 fitting, and their IR-to-millimeter are actually well fitted, leaving the stellar part poorly constrained (CenA and NGC 0253). In comparison, there are 12 poor/failed cases in CIGALE fitting, and 4 in MAGPHYS fitting. The main reason for these poor/failed cases is likely the energy balance forced in MAGPHYS and CIGALE. In these cases, the stellar part of the SED fitting gives a dust attenuation that cannot fully balance the far-IR/millimeter emission, and this is also mentioned in other studies of extremely dust-obscured high-redshift galaxies (e.g., Casey et al. 2017; Miettinen et al. 2017b, 2017a; Simpson et al. 2017). Except for these poor/failed fittings, the fitted IR luminosities and stellar masses reasonably agree within about 0.3 dex.

In the comparison of $\langle U \rangle$ in Figure 12, we excluded the 12 sources with reduced-$\chi^2 > 10$ in CIGALE fitting. Although most sources have consistent $\langle U \rangle$, a small number of sources do not have consistent $\langle U \rangle$, and they mostly come from the V20 subsample. This is mainly because they have very poor IR photometry except for one or two submillimeter interferometry photometries. But we chose to skip these interferometry photometries in our CIGALE fitting tests owing to the filter setting. Adding a fake filter in CIGALE and rerunning the fitting for each of these sources are required in order to fit the submillimeter interferometry photometry, and then more

[29] All SED fitting figures are available at 10.5281/zenodo.3958271.

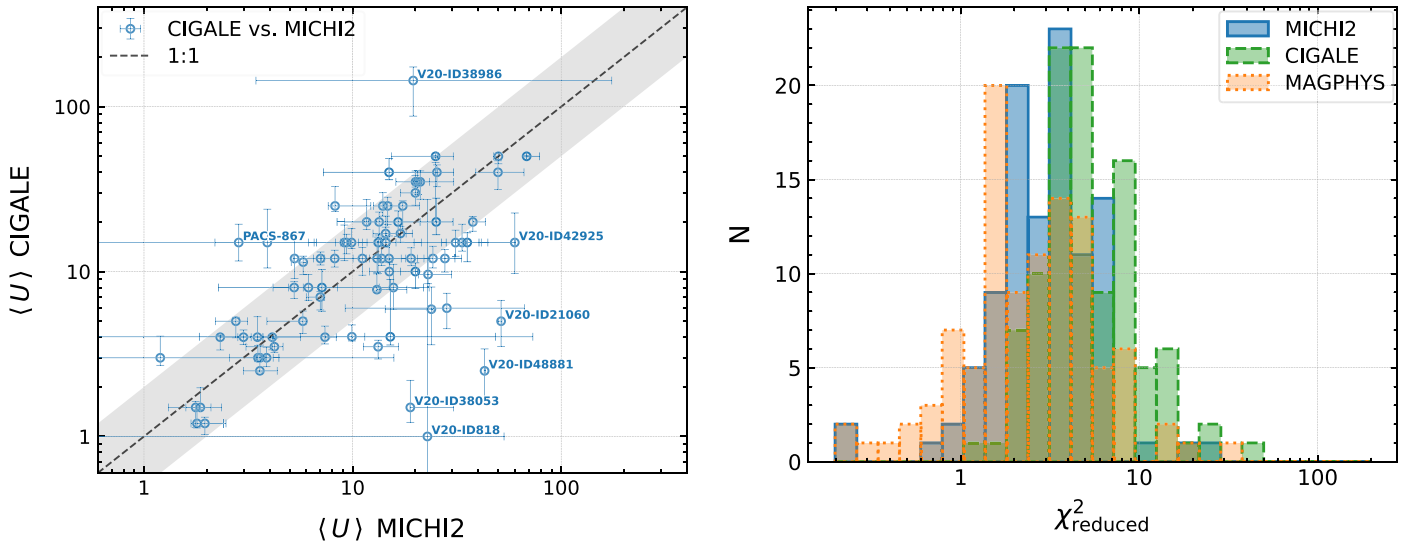

Figure 12. Left panel: comparison of the fitted $\langle U \rangle$ from MICHI2 and CIGALE. Symbols are similar to Figure 11, except that data points with reduced-$\chi^2 > 10$ are excluded. Right panel: histograms of the reduced-χ^2 from MICHI2, CIGALE, and MAGPHYS SED fittings. Given that our fittings span from UV/optical to millimeter/radio wavelengths, a reduced-χ^2 larger than unity is not unexpected. A value of a few still indicates a reasonable fitting in our cases, but >10 usually means poor or failed fitting.

consistent results are expected. Therefore, these comparisons show that for sources with good reduced-χ^2 and photometry data MICHI2 and CIGALE have similar constraints on $\langle U \rangle$.

Appendix D
Gas Modeling Prediction on Line Optical Depth and [C I]/CO Line Ratio

We present the predicted [C I] ($^3P_1 - {}^3P_0$) (hereafter [C I] (1–0)) and CO (1–0) line optical depths and the [C I] (1–0)/CO (1–0) line ratio in surface brightness unit ($R'_{\rm CICO}$) in Figures 13–15. The optical depths shown in Figure 13 agree with normal conditions where CO (1–0) is optically thick, while [C I] (1–0) is roughly optically thin or has $\tau \sim 1$.

Figures 14 and 15 show $R'_{\rm CICO}$ as a function of one-zone cloud molecular gas density and mean molecular gas density of the composite PDF, respectively. Similarly to Figures 4 and 5, we show our prediction at four redshifts, $z = 0$, 1.5, 4, and 6, and with three representative $T_{\rm kin} = 25$, 50, and 100 K. $R'_{\rm CICO}$ increases with $n_{\rm H_2}$ or $\langle n_{\rm H_2} \rangle$ but strongly decreases with $T_{\rm kin}$ at intermediate $n_{\rm H_2} \sim 10^{3-4}$ cm^{-3}. Future study of this line ratio with our gas modeling will shed light on how to better constrain $T_{\rm kin}$ and $\langle n_{\rm H_2} \rangle$.

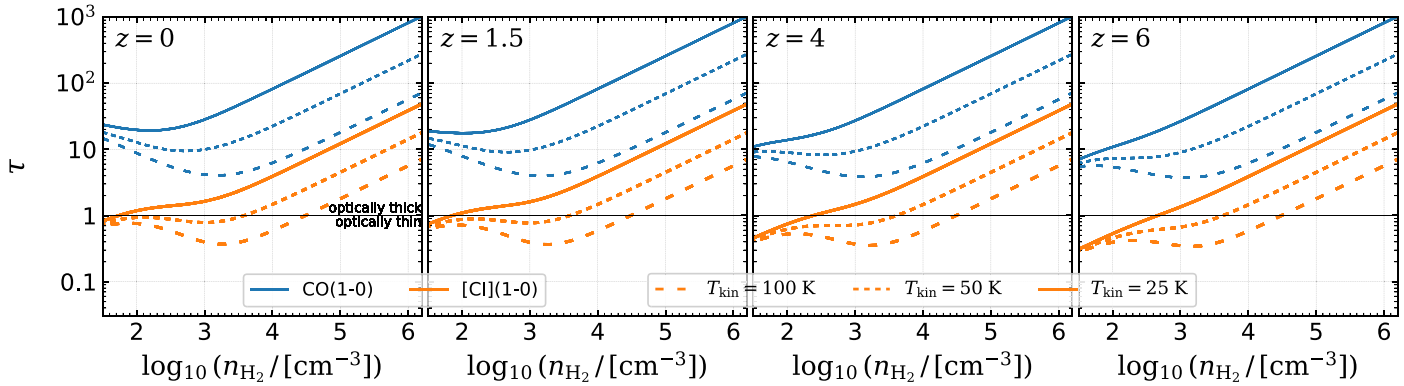

Figure 13. Optical depths (τ) of CO (1–0) and [C I] (1–0) as a function of the gas density of each single LVG (one-zone) model in four redshift panels. Blue lines are CO (1–0), and orange lines are [C I] (1–0). Line styles (solid, short-dashed, and long-dashed) represent different gas kinetic temperatures as labeled. These show that the derived optical depths from our models (Section 5) roughly agree with observations that usually show optically thin ($\tau \sim 1$) [C I] (1–0) and optically thick CO (1–0).

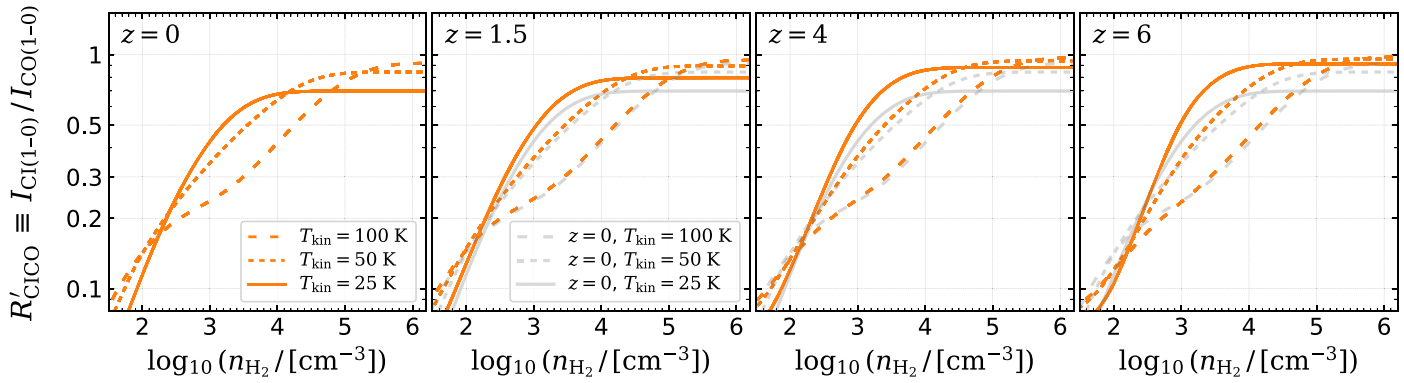

Figure 14. Ratio between [C I] (1–0) and CO (1–0) line surface brightness from our single LVG one-zone models. Lines and symbols are similar to those in Figure 4, but note that the ratio in Figure 4 is flux ratio while here we show the surface brightness ratio ($R'_{\rm C\,I/CO} \equiv L'_{\rm [C\,I](1-0)}/L'_{\rm CO(1-0)}$).

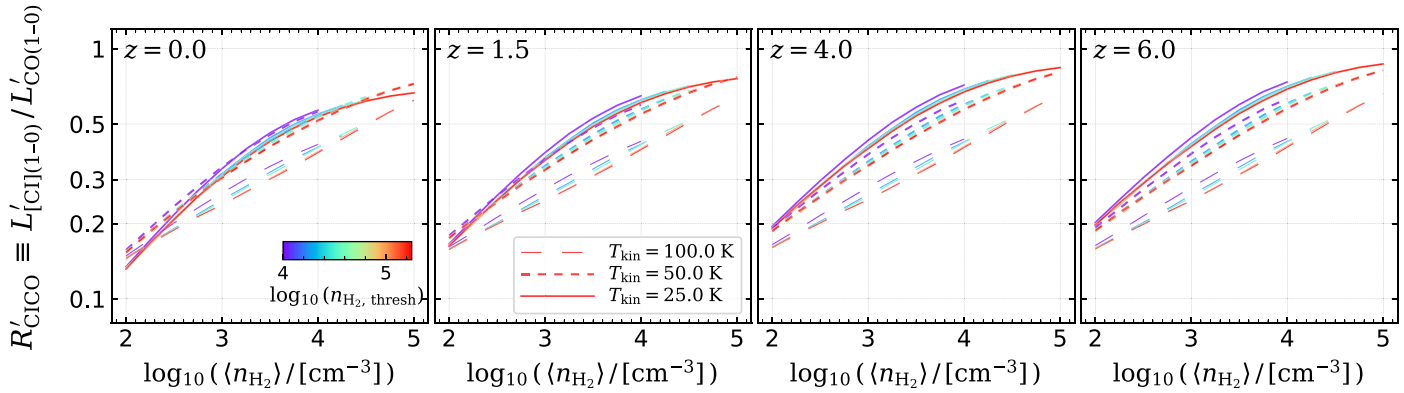

Figure 15. Ratio between [C I] (1–0) and CO (1–0) line surface brightness from our density–PDF gas modeling. Lines and symbols are similar to those in Figure 5 (see also the note about the different ratio definition in the caption of Figure 14).

ORCID iDs

Daizhong Liu https://orcid.org/0000-0001-9773-7479
Emanuele Daddi https://orcid.org/0000-0002-3331-9590
Eva Schinnerer https://orcid.org/0000-0002-3933-7677
Toshiki Saito https://orcid.org/0000-0002-2501-9328
Adam Leroy https://orcid.org/0000-0002-2545-1700
John D. Silverman https://orcid.org/0000-0002-0000-6977
Francesco Valentino https://orcid.org/0000-0001-6477-4011
Georgios E. Magdis https://orcid.org/0000-0002-4872-2294
Yu Gao https://orcid.org/0000-0003-0007-2197
Shuowen Jin https://orcid.org/0000-0002-8412-7951
Annagrazia Puglisi https://orcid.org/0000-0001-9369-1805
Brent Groves https://orcid.org/0000-0002-9768-0246

References

Aalto, S., Booth, R. S., Black, J. H., & Johansson, L. E. B. 1995, A&A, 300, 369
Alatalo, K., Blitz, L., Young, L. M., et al. 2011, ApJ, 735, 88
Albrecht, M., Krügel, E., & Chini, R. 2007, A&A, 462, 575

Aniano, G., Draine, B. T., Calzetti, D., et al. 2012, ApJ, 756, 138
Aniano, G., Draine, B. T., Hunt, L. K., et al. 2020, ApJ, 889, 150
Aravena, M., Bertoldi, F., Schinnerer, E., et al. 2008, A&A, 491, 173
Armus, L., Mazzarella, J. M., Evans, A. S., et al. 2009, PASP, 121, 559
Arnouts, S., Cristiani, S., Moscardini, L., et al. 1999, MNRAS, 310, 540
Baan, W. A., Henkel, C., Loenen, A. F., Baudry, A., & Wiklind, T. 2008, A&A, 477, 747
Battisti, A. J., da Cunha, E., Grasha, K., et al. 2019, ApJ, 882, 61
Bayet, E., Gerin, M., Phillips, T. G., & Contursi, A. 2004, A&A, 427, 45
Bayet, E., Gerin, M., Phillips, T. G., & Contursi, A. 2006, A&A, 460, 467
Bayet, E., Gerin, M., Phillips, T. G., & Contursi, A. 2009, MNRAS, 399, 264
Bertoldi, F., & McKee, C. F. 1992, ApJ, 395, 140
Béthermin, M., Daddi, E., Magdis, G., et al. 2015, A&A, 573, A113
Bigiel, F., Leroy, A., Walter, F., et al. 2008, AJ, 136, 2846
Bolatto, A. D., Wolfire, M., & Leroy, A. K. 2013, ARA&A, 51, 207
Boogaard, L. A., Decarli, R., González-López, J., et al. 2019, ApJ, 882, 140
Boquien, M., Burgarella, D., Roehlly, Y., et al. 2019, A&A, 622, A103
Bothwell, M. S., Aguirre, J. E., Aravena, M., et al. 2017, MNRAS, 466, 2825
Bournaud, F., Daddi, E., Weiß, A., et al. 2015, A&A, 575, A56
Bradford, C. M., Nikola, T., Stacey, G. J., et al. 2003, ApJ, 586, 891
Braine, J., & Combes, F. 1992, A&A, 264, 433
Brauher, J. R., Dale, D. A., & Helou, G. 2008, ApJS, 178, 280
Brouillet, N., & Schilke, P. 1993, A&A, 277, 381
Brown, M. J. I., Moustakas, J., Smith, J. D. T., et al. 2014, ApJS, 212, 18
Bruzual, G., & Charlot, S. 2003, MNRAS, 344, 1000
Burgarella, D., Buat, V., & Iglesias-Páramo, J. 2005, MNRAS, 360, 1413
Calabrò, A., Daddi, E., Puglisi, A., et al. 2019, A&A, 623, A64
Calzetti, D., Armus, L., Bohlin, R. C., et al. 2000, ApJ, 533, 682
Cañameras, R., Yang, C., Nesvadba, N. P. H., et al. 2018, A&A, 620, A61
Carilli, C. L., Daddi, E., Riechers, D., et al. 2010, ApJ, 714, 1407
Carilli, C. L., & Walter, F. 2013, ARA&A, 51, 105
Casey, C. M., Cooray, A., Killi, M., et al. 2017, ApJ, 840, 101
Chabrier, G. 2003, PASP, 115, 763
Chang, Y.-Y., van der Wel, A., da Cunha, E., & Rix, H.-W. 2015, ApJS, 219, 8
Chapman, S. C., Blain, A. W., Smail, I., & Ivison, R. J. 2005, ApJ, 622, 772
Charlot, S., & Fall, S. M. 2000, ApJ, 539, 718
Chevance, M., Kruijssen, J. M. D., Hygate, A. P. S., et al. 2020, MNRAS, 493, 2872
Chu, J. K., Sanders, D. B., Larson, K. L., et al. 2017, ApJS, 229, 25
Ciesla, L., Boquien, M., Boselli, A., et al. 2014, A&A, 565, A128
Ciesla, L., Charmandaris, V., Georgakakis, A., et al. 2015, A&A, 576, A10
Clark, C. J. R., Verstocken, S., Bianchi, S., et al. 2018, A&A, 609, A37
Clements, D. L., Pearson, C., Farrah, D., et al. 2018, MNRAS, 475, 2097
Combes, F. 2018, A&A Rv, 26, 5
Condon, J. J., Anderson, M. L., & Helou, G. 1991, ApJ, 376, 95
Conroy, C., & Gunn, J. E. 2010a, ApJ, 712, 833
Conroy, C., & Gunn, J. E. 2010b, FSPS: Flexible Stellar Population Synthesis v2.3., Astrophysics Source Code Library, ascl:1010.043
Conroy, C., Gunn, J. E., & White, M. 2009, ApJ, 699, 486
Cooray, A., Calanog, J., Wardlow, J. L., et al. 2014, ApJ, 790, 40
Coppin, K. E. K., Chapman, S. C., Smail, I., et al. 2010, MNRAS, 407, L103
Cortzen, I., Magdis, G. E., Valentino, F., et al. 2020, A&A, 634, L14
Cox, P., Krips, M., Neri, R., et al. 2011, ApJ, 740, 63
Curran, S. J., Polatidis, A. G., Aalto, S., & Booth, R. S. 2001, A&A, 368, 824
da Cunha, E., Charlot, S., & Elbaz, D. 2008, MNRAS, 388, 1595
da Cunha, E., Walter, F., Smail, I. R., et al. 2015, ApJ, 806, 110
Daddi, E., Bournaud, F., Walter, F., et al. 2010a, ApJ, 713, 686
Daddi, E., Cimatti, A., Renzini, A., et al. 2004, ApJ, 617, 746
Daddi, E., Dannerbauer, H., Elbaz, D., et al. 2008, ApJL, 673, L21
Daddi, E., Dannerbauer, H., Liu, D., et al. 2015, A&A, 577, A46
Daddi, E., Dannerbauer, H., Stern, D., et al. 2009, ApJ, 694, 1517
Daddi, E., Dickinson, M., Morrison, G., et al. 2007, ApJ, 670, 156
Daddi, E., Elbaz, D., Walter, F., et al. 2010b, ApJL, 714, L118
Dale, D. A., Aniano, G., Engelbracht, C. W., et al. 2012, ApJ, 745, 95
Dale, D. A., Cook, D. O., Roussel, H., et al. 2017, ApJ, 837, 90
Dale, D. A., & Helou, G. 2002, ApJ, 576, 159
Dale, D. A., Helou, G., Contursi, A., Silbermann, N. A., & Kolhatkar, S. 2001, ApJ, 549, 215
de los Reyes, M. A. C., & Kennicutt, R. C. J. 2019, ApJ, 872, 16
Downes, D., Radford, S. J. E., Guilloteau, S., et al. 1992, A&A, 262, 424
Draine, B. T., Aniano, G., Krause, O., et al. 2014, ApJ, 780, 172
Draine, B. T., Dale, D. A., Bendo, G., et al. 2007, ApJ, 663, 866
Draine, B. T., & Li, A. 2007, ApJ, 657, 810
Druard, C., Braine, J., Schuster, K. F., et al. 2014, A&A, 567, A118
Eckart, A., Cameron, M., Rothermel, H., et al. 1990, ApJ, 363, 451
Elbaz, D., Daddi, E., Le Borgne, D., et al. 2007, A&A, 468, 33
Elbaz, D., Dickinson, M., Hwang, H. S., et al. 2011, A&A, 533, A119
Elmegreen, B. G. 2002, ApJ, 564, 773
Elmegreen, B. G. 2018, ApJ, 854, 16
Engel, H., Tacconi, L. J., Davies, R. I., et al. 2010, ApJ, 724, 233
Federrath, C., & Klessen, R. S. 2013, ApJ, 763, 51
Feldmann, R., Gnedin, N. Y., & Kravtsov, A. V. 2011, ApJ, 732, 115
Fixsen, D. J., Bennett, C. L., & Mather, J. C. 1999, ApJ, 526, 207
Fritz, J., Franceschini, A., & Hatziminaoglou, E. 2006, MNRAS, 366, 767
Galliano, F., Hony, S., Bernard, J. P., et al. 2011, A&A, 536, A88
Gao, Y., & Solomon, P. M. 2004a, ApJ, 606, 271
Gao, Y., & Solomon, P. M. 2004b, ApJS, 152, 63
Garay, G., Mardones, D., & Mirabel, I. F. 1993, A&A, 277, 405
Gardan, E., Braine, J., Schuster, K. F., Brouillet, N., & Sievers, A. 2007, A&A, 473, 91
Geach, J. E., Dunlop, J. S., Halpern, M., et al. 2017, MNRAS, 465, 1789
Genzel, R., Tacconi, L. J., Gracia-Carpio, J., et al. 2010, MNRAS, 407, 2091
Glover, S. C. O., & Clark, P. C. 2012, MNRAS, 421, 116
Glover, S. C. O., Clark, P. C., Micic, M., & Molina, F. 2015, MNRAS, 448, 1607
Glover, S. C. O., & Smith, R. J. 2016, MNRAS, 462, 3011
Goldreich, P., & Kwan, J. 1974, ApJ, 189, 441
Gratier, P., Braine, J., Rodriguez-Fernandez, N. J., et al. 2010, A&A, 522, A3
Greve, T. R., Leonidaki, I., Xilouris, E. M., et al. 2014, ApJ, 794, 142
Greve, T. R., Papadopoulos, P. P., Gao, Y., & Radford, S. J. E. 2009, ApJ, 692, 1432
Greve, T. R., Pope, A., Scott, D., et al. 2008, MNRAS, 389, 1489
Griffin, M. J., Abergel, A., Abreu, A., et al. 2010, A&A, 518, L3
Guesten, R., Serabyn, E., Kasemann, C., et al. 1993, ApJ, 402, 537
Hailey-Dunsheath, S., Nikola, T., Stacey, G. J., et al. 2008, ApJL, 689, L109
Hailey-Dunsheath, S., Sturm, E., Fischer, J., et al. 2012, ApJ, 755, 57
Harrington, K. C., Vishwas, A., Weiß, A., et al. 2019, MNRAS, 488, 1489
Harrington, K. C., Weiss, A., Yun, M. S., et al. 2021, ApJ, 908, 95
Harrington, K. C., Yun, M. S., Magnelli, B., et al. 2018, MNRAS, 474, 3866
Harris, A. I., Hills, R. E., Stutzki, J., et al. 1991, ApJL, 382, L75
Harrison, A., Henkel, C., & Russell, A. 1999, MNRAS, 303, 157
Hennebelle, P., & Chabrier, G. 2011, ApJL, 743, L29
Herrero-Illana, R., Privon, G. C., Evans, A. S., et al. 2019, A&A, 628, A71
Heyer, M., & Dame, T. M. 2015, ARA&A, 53, 583
Hughes, A., Meidt, S. E., Schinnerer, E., et al. 2013, ApJ, 779, 44
Hughes, A., Wong, T., Ott, J., et al. 2010, MNRAS, 406, 2065
Hwang, H. S., Elbaz, D., Magdis, G., et al. 2010, MNRAS, 409, 75
Ilbert, O., Arnouts, S., McCracken, H. J., et al. 2006, A&A, 457, 841
Ilbert, O., McCracken, H. J., Le Fèvre, O., et al. 2013, A&A, 556, A55
Israel, F. P. 1997, A&A, 317, 65
Israel, F. P. 2005, A&A, 438, 855
Israel, F. P. 2009a, A&A, 493, 525
Israel, F. P. 2009b, A&A, 506, 689
Israel, F. P., & Baas, F. 2001, A&A, 371, 433
Israel, F. P., & Baas, F. 2002, A&A, 383, 82
Israel, F. P., & Baas, F. 2003, A&A, 404, 495
Israel, F. P., Güsten, R., Meijerink, R., et al. 2014, A&A, 562, A96
Israel, F. P., Rosenberg, M. J. F., & van der Werf, P. 2015, A&A, 578, A95
Israel, F. P., Tilanus, R. P. J., & Baas, F. 2006, A&A, 445, 907
Israel, F. P., White, G. J., & Baas, F. 1995, A&A, 302, 343
Ivison, R. J., Magnelli, B., Ibar, E., et al. 2010, A&A, 518, L31
Jarrett, T. H., Chester, T., Cutri, R., Schneider, S. E., & Huchra, J. P. 2003, AJ, 125, 525
Jiao, Q., Zhao, Y., Lu, N., et al. 2019, ApJ, 880, 133
Jiao, Q., Zhao, Y., Zhu, M., et al. 2017, ApJL, 840, L18
Jin, S., Daddi, E., Liu, D., et al. 2018, ApJ, 864, 56
Jin, S., Daddi, E., Magdis, G. E., et al. 2019, ApJ, 887, 144
Kainulainen, J., & Federrath, C. 2017, A&A, 608, L3
Kainulainen, J., & Tan, J. C. 2013, A&A, 549, A53
Kamenetzky, J., Glenn, J., Maloney, P. R., et al. 2011, ApJ, 731, 83
Kamenetzky, J., Glenn, J., Rangwala, N., et al. 2012, ApJ, 753, 70
Kamenetzky, J., Privon, G. C., & Narayanan, D. 2018, ApJ, 859, 9
Kamenetzky, J., Rangwala, N., & Glenn, J. 2017, MNRAS, 471, 2917
Kamenetzky, J., Rangwala, N., Glenn, J., Maloney, P. R., & Conley, A. 2014, ApJ, 795, 174
Kamenetzky, J., Rangwala, N., Glenn, J., Maloney, P. R., & Conley, A. 2016, ApJ, 829, 93
Kennicutt, R. C., Calzetti, D., Aniano, G., et al. 2011, PASP, 123, 1347
Kennicutt, R. C., & Evans, N. J. 2012, ARA&A, 50, 531
Kennicutt, R. C., Jr. 1998, ApJ, 498, 541
Klessen, R. S., Heitsch, F., & Mac Low, M.-M. 2000, ApJ, 535, 887
Komugi, S., Sofue, Y., Kohno, K., et al. 2008, ApJS, 178, 225

Kovács, A., Chapman, S. C., Dowell, C. D., et al. 2006, ApJ, 650, 592
Kreckel, K., Faesi, C., Kruijssen, J. M. D., et al. 2018, ApJL, 863, L21
Kritsuk, A. G., Ustyugov, S. D., & Norman, M. L. 2017, NJPh, 19, 065003
Krumholz, M. R., & McKee, C. F. 2005, ApJ, 630, 250
Krumholz, M. R., & Thompson, T. A. 2007, ApJ, 669, 289
Kuno, N., Sato, N., Nakanishi, H., et al. 2007, PASJ, 59, 117
Laigle, C., McCracken, H. J., Ilbert, O., et al. 2016, ApJS, 224, 24
Laporte, N., Pérez-Fournon, I., Calanog, J. A., et al. 2015, ApJ, 810, 130
Larson, K. L., Sanders, D. B., Barnes, J. E., et al. 2016, ApJ, 825, 128
Leroy, A., Bolatto, A., Stanimirovic, S., et al. 2007, ApJ, 658, 1027
Leroy, A. K., Bolatto, A., Gordon, K., et al. 2011, ApJ, 737, 12
Leroy, A. K., Hughes, A., Schruba, A., et al. 2016, ApJ, 831, 16
Leroy, A. K., Usero, A., Schruba, A., et al. 2017, ApJ, 835, 217
Leroy, A. K., Walter, F., Bigiel, F., et al. 2009, AJ, 137, 4670
Leroy, A. K., Walter, F., Brinks, E., et al. 2008, AJ, 136, 2782
Leroy, A. K., Walter, F., Sandstrom, K., et al. 2013, AJ, 146, 19
Leung, C. M., & Liszt, H. S. 1976, ApJ, 208, 732
Li, A., & Draine, B. T. 2002, ApJ, 576, 762
Lisenfeld, U., Isaak, K. G., & Hills, R. 2000, MNRAS, 312, 433
Liu, D., Daddi, E., Dickinson, M., et al. 2018, ApJ, 853, 172
Liu, D., Lang, P., Magnelli, B., et al. 2019a, ApJS, 244, 40
Liu, D., Schinnerer, E., Groves, B., et al. 2019b, ApJ, 887, 235
Liu, D. D., Gao, Y., Isaak, K., et al. 2015, ApJL, 810, L14
Lo Faro, B., Buat, V., Roehlly, Y., et al. 2017, MNRAS, 472, 1372
Lombardi, M., Alves, J., & Lada, C. J. 2015, A&A, 576, L1
Lombardi, M., Bouy, H., Alves, J., & Lada, C. J. 2014, A&A, 566, A45
Lu, N., Zhao, Y., Díaz-Santos, T., et al. 2017, ApJS, 230, 1
Lu, N., Zhao, Y., Xu, C. K., et al. 2014, ApJL, 787, L23
Lu, N., Zhao, Y., Xu, C. K., et al. 2015, ApJL, 802, L11
Lundgren, A. A., Wiklind, T., Olofsson, H., & Rydbeck, G. 2004, A&A, 413, 505
Lutz, D., Poglitsch, A., Altieri, B., et al. 2011, A&A, 532, A90
Magdis, G. E., Daddi, E., Béthermin, M., et al. 2012, ApJ, 760, 6
Magdis, G. E., Elbaz, D., Hwang, H. S., et al. 2010, MNRAS, 409, 22
Magdis, G. E., Rigopoulou, D., Daddi, E., et al. 2017, A&A, 603, A93
Magnelli, B., Ivison, R. J., Lutz, D., et al. 2015, A&A, 573, A45
Magnelli, B., Lutz, D., Berta, S., et al. 2010, A&A, 518, L28
Magnelli, B., Lutz, D., Saintonge, A., et al. 2014, A&A, 561, A86
Magnelli, B., Saintonge, A., Lutz, D., et al. 2012, A&A, 548, A22
Mao, R. Q., Henkel, C., Schulz, A., et al. 2000, A&A, 358, 433
Mashian, N., Sturm, E., Sternberg, A., et al. 2015, ApJ, 802, 81
Mathis, J. S., Mezger, P. G., & Panagia, N. 1983, A&A, 128, 212
McCracken, H. J., Milvang-Jensen, B., Dunlop, J., et al. 2012, A&A, 544, A156
Meijerink, R., Kristensen, L. E., Weiß, A., et al. 2013, ApJL, 762, L16
Miettinen, O., Delvecchio, I., Smolčić, V., et al. 2017a, A&A, 606, A17
Miettinen, O., Novak, M., Smolčić, V., et al. 2017b, A&A, 602, A54
Mullaney, J. R., Alexander, D. M., Goulding, A. D., & Hickox, R. C. 2011, MNRAS, 414, 1082
Muzzin, A., Marchesini, D., Stefanon, M., et al. 2013, ApJ, 777, 18
Narayanan, D., & Krumholz, M. R. 2014, MNRAS, 442, 1411
Naylor, D. A., Baluteau, J.-P., Barlow, M. J., et al. 2010, Proc. SPIE, 7731, 773116
Noeske, K. G., Weiner, B. J., Faber, S. M., et al. 2007, ApJL, 660, L43
Noll, S., Burgarella, D., Giovannoli, E., et al. 2009, A&A, 507, 1793
Nordlund, Å., & Padoan, P. 1999, in The Density PDFs of Supersonic Random Flows, ed. J. Franco & A. Carraminana (Cambridge: Cambridge Univ. Press), 218
Ostriker, E. C., Gammie, C. F., & Stone, J. M. 1999, ApJ, 513, 259
Ostriker, E. C., Stone, J. M., & Gammie, C. F. 2001, ApJ, 546, 980
Padoan, P., Haugbølle, T., & Nordlund, Å. 2012, ApJL, 759, L27
Padoan, P., Jimenez, R., Juvela, M., & Nordlund, Å. 2004a, ApJL, 604, L49
Padoan, P., Jimenez, R., Nordlund, Å., & Boldyrev, S. 2004b, PhRvL, 92, 191102
Padoan, P., & Nordlund, Å. 2002, ApJ, 576, 870
Padoan, P., & Nordlund, Å. 2011, ApJ, 730, 40
Panuzzo, P., Rangwala, N., Rykala, A., et al. 2010, A&A, 518, L37
Papadopoulos, P. P. 2007, ApJ, 656, 792
Papadopoulos, P. P., Isaak, K., & van der Werf, P. 2010a, ApJ, 711, 757
Papadopoulos, P. P., Isaak, K. G., & van der Werf, P. P. 2007, ApJ, 668, 815
Papadopoulos, P. P., Kovacs, A., Evans, A. S., & Barthel, P. 2008, A&A, 491, 483
Papadopoulos, P. P., & Seaquist, E. R. 1999, ApJ, 516, 114
Papadopoulos, P. P., van der Werf, P., Isaak, K., & Xilouris, E. M. 2010b, ApJ, 715, 775
Papadopoulos, P. P., van der Werf, P. P., Xilouris, E. M., et al. 2012, MNRAS, 426, 2601
Papadopoulos, P. P., Zhang, Z.-Y., Xilouris, E. M., et al. 2014, ApJ, 788, 153
Penner, K., Pope, A., Chapin, E. L., et al. 2011, MNRAS, 410, 2749
Pereira-Santaella, M., Spinoglio, L., Busquet, G., et al. 2013, ApJ, 768, 55
Perera, T. A., Chapin, E. L., Austermann, J. E., et al. 2008, MNRAS, 391, 1227
Pety, J., Schinnerer, E., Leroy, A. K., et al. 2013, ApJ, 779, 43
Pilbratt, G. L., Riedinger, J. R., Passvogel, T., et al. 2010, A&A, 518, L1
Pineda, J. L., Ott, J., Klein, U., et al. 2009, ApJ, 703, 736
Popping, G., Narayanan, D., Somerville, R. S., Faisst, A. L., & Krumholz, M. R. 2019, MNRAS, 482, 4906
Popping, G., van Kampen, E., Decarli, R., et al. 2016, MNRAS, 461, 93
Press, W. H., Teukolsky, S. A., Vetterling, W. T., & Flannery, B. P. 1992, Numerical Recipes in C. The Art of Scientific Computing (2nd ed.; Cambridge: Cambridge Univ. Press)
Rangwala, N., Maloney, P. R., Glenn, J., et al. 2011, ApJ, 743, 94
Raskutti, S., Ostriker, E. C., & Skinner, M. A. 2017, ApJ, 850, 112
Rémy-Ruyer, A., Madden, S. C., Galliano, F., et al. 2014, A&A, 563, A31
Rémy-Ruyer, A., Madden, S. C., Galliano, F., et al. 2015, A&A, 582, A121
Renaud, F., Bournaud, F., Agertz, O., et al. 2019a, A&A, 625, A65
Renaud, F., Bournaud, F., Daddi, E., & Weiß, A. 2019b, A&A, 621, A104
Riechers, D. A., Bradford, C. M., Clements, D. L., et al. 2013, Natur, 496, 329
Riechers, D. A., Capak, P. L., Carilli, C. L., et al. 2010, ApJL, 720, L131
Rigopoulou, D., Hurley, P. D., Swinyard, B. M., et al. 2013, MNRAS, 434, 2051
Roseboom, I. G., Oliver, S. J., Kunz, M., et al. 2010, MNRAS, 409, 48
Rosenberg, M. J. F., Kazandjian, M. V., van der Werf, P. P., et al. 2014a, A&A, 564, A126
Rosenberg, M. J. F., Meijerink, R., Israel, F. P., et al. 2014b, A&A, 568, A90
Rosenberg, M. J. F., van der Werf, P. P., Aalto, S., et al. 2015, ApJ, 801, 72
Saito, T., Iono, D., Xu, C. K., et al. 2017, ApJ, 835, 174
Salim, D. M., Federrath, C., & Kewley, L. J. 2015, ApJL, 806, L36
Sandqvist, A., Joersaeter, S., & Lindblad, P. O. 1995, A&A, 295, 585
Sandstrom, K. M., Leroy, A. K., Walter, F., et al. 2013, ApJ, 777, 5
Schinnerer, E., Hughes, A., Leroy, A., et al. 2019, ApJ, 887, 49
Schinnerer, E., Meidt, S. E., Colombo, D., et al. 2017, ApJ, 836, 62
Schinnerer, E., Meidt, S. E., Pety, J., et al. 2013, ApJ, 779, 42
Schirm, M. R. P., Wilson, C. D., Kamenetzky, J., et al. 2017, MNRAS, 470, 4989
Schirm, M. R. P., Wilson, C. D., Parkin, T. J., et al. 2014, ApJ, 781, 101
Schmidt, M. 1959, ApJ, 129, 243
Schreiber, C., Elbaz, D., Pannella, M., et al. 2018, A&A, 609, A30
Schruba, A., Leroy, A. K., Walter, F., et al. 2011, AJ, 142, 37
Sheffer, Y., Rogers, M., Federman, S. R., et al. 2008, ApJ, 687, 1075
Shetty, R., Clark, P. C., & Klessen, R. S. 2014a, MNRAS, 442, 2208
Shetty, R., Kelly, B. C., & Bigiel, F. 2013, MNRAS, 430, 288
Shetty, R., Kelly, B. C., Rahman, N., et al. 2014b, MNRAS, 437, L61
Shirley, Y. L. 2015, PASP, 127, 299
Shirley, Y. L., Evans, N. J., II, Mueller, K. E., Knez, C., & Jaffe, D. T. 2002, in ASP Conf. Ser. 267, Hot Star Workshop III: The Earliest Phases of Massive Star Birth, ed. P. Crowther (San Francisco, CA: ASP), 417
Silverman, J. D., Daddi, E., Rodighiero, G., et al. 2015a, ApJL, 812, L23
Silverman, J. D., Kashino, D., Sanders, D., et al. 2015b, ApJS, 220, 12
Simpson, J. M., Smail, I., Swinbank, A. M., et al. 2017, ApJ, 839, 58
Skelton, R. E., Whitaker, K. E., Momcheva, I. G., et al. 2014, ApJS, 214, 24
Smith, R. J., Glover, S. C. O., Clark, P. C., Klessen, R. S., & Springel, V. 2014a, MNRAS, 441, 1628
Smith, R. J., Glover, S. C. O., & Klessen, R. S. 2014b, MNRAS, 445, 2900
Smith, R. J., Glover, S. C. O., Klessen, R. S., & Fuller, G. A. 2016, MNRAS, 455, 3640
Smith, R. J., Treß, R. G., Sormani, M. C., et al. 2020, MNRAS, 492, 1594
Solomon, P. M., & Vanden Bout, P. A. 2005, ARA&A, 43, 677
Speagle, J. S., Steinhardt, C. L., Capak, P. L., & Silverman, J. D. 2014, ApJS, 214, 15
Spinoglio, L., Pereira-Santaella, M., Busquet, G., et al. 2012, ApJ, 758, 108
Stutzki, J. 2001, ApSSS, 277, 39
Sun, J., Leroy, A. K., Ostriker, E. C., et al. 2020, ApJ, 892, 148
Sun, J., Leroy, A. K., Schruba, A., et al. 2018, ApJ, 860, 172
Symeonidis, M., Page, M. J., Seymour, N., et al. 2009, MNRAS, 397, 1728
Symeonidis, M., Page, M. J., & Seymour, N. 2011, MNRAS, 411, 983
Symeonidis, M., Vaccari, M., Berta, S., et al. 2013, MNRAS, 431, 2317
Tacconi, L. J., Genzel, R., Smail, I., et al. 2008, ApJ, 680, 246
Tan, Q., Daddi, E., Magdis, G., et al. 2014, A&A, 569, A98
Tassis, K., Christie, D. A., Urban, A., et al. 2010, MNRAS, 408, 1089
Tress, R. G., Smith, R. J., Sormani, M. C., et al. 2020, MNRAS, 492, 2973

Usero, A., Leroy, A. K., Walter, F., et al. 2015, AJ, 150, 115
Valentino, F., Daddi, E., Puglisi, A., et al. 2020a, A&A, 641, A155
Valentino, F., Magdis, G. E., Daddi, E., et al. 2018, ApJ, 869, 27
Valentino, F., Magdis, G. E., Daddi, E., et al. 2020b, ApJ, 890, 24
van der Tak, F. F. S., Black, J. H., Schöier, F. L., Jansen, D. J., & van Dishoeck, E. F. 2007, A&A, 468, 627
van der Werf, P. P., Isaak, K. G., Meijerink, R., et al. 2010, A&A, 518, L42
van Dishoeck, E. F., & Black, J. H. 1987, in NATO ASIC Proc. 210: Physical Processes in Interstellar Clouds, ed. G. E. Morfill & M. Scholer (Dordrecht: Reidel), 241
van Dishoeck, E. F., & Black, J. H. 1988, ApJ, 334, 771
Vázquez-Semadeni, E., & García, N. 2001, ApJ, 557, 727
Walter, F., Decarli, R., Carilli, C., et al. 2012, Natur, 486, 233
Wang, M., Henkel, C., Chin, Y.-N., et al. 2004, A&A, 422, 883
Weiß, A., Neininger, N., Hüttemeister, S., & Klein, U. 2001, A&A, 365, 571
Weiß, A., Walter, F., & Scoville, N. Z. 2005, A&A, 438, 533
Wild, W., Harris, A. I., Eckart, A., et al. 1992, A&A, 265, 447
Wilson, C. D., Elmegreen, B. G., Bemis, A., & Brunetti, N. 2019, ApJ, 882, 5
Wilson, C. D., Petitpas, G. R., Iono, D., et al. 2008, ApJS, 178, 189
Wong, T., & Blitz, L. 2002, ApJ, 569, 157
Wong, T., Hughes, A., Ott, J., et al. 2011, ApJS, 197, 16
Wu, R., Madden, S. C., Galliano, F., et al. 2015, A&A, 575, A88
Yang, C., Omont, A., Beelen, A., et al. 2017, A&A, 608, A144
Yang, G., Boquien, M., Buat, V., et al. 2020, MNRAS, 491, 740
Yao, L., Seaquist, E. R., Kuno, N., & Dunne, L. 2003, ApJ, 588, 771
Young, J. S., & Scoville, N. Z. 1991, ARA&A, 29, 581
Young, L. M., Bureau, M., Davis, T. A., et al. 2011, MNRAS, 414, 940
Yun, M. S., Reddy, N. A., & Condon, J. J. 2001, ApJ, 554, 803
Zhang, M., Kainulainen, J., Mattern, M., Fang, M., & Henning, T. 2019, A&A, 622, A52
Zhang, Z.-Y., Gao, Y., Henkel, C., et al. 2014, ApJL, 784, L31
Zhao, Y., Lu, N., Díaz-Santos, T., et al. 2020, ApJ, 892, 145
Zhu, M., Seaquist, E. R., & Kuno, N. 2003, ApJ, 588, 243